



Title	Heating duration of igneous rim formation on a chondrule in the Northwest Africa 3118 CV3(oxA) carbonaceous chondrite inferred from micro-scale migration of the oxygen isotopes
Author(s)	Matsuda, Nozomi; Sakamoto, Naoya; Tachibana, Shogo; Yurimoto, Hisayoshi
Citation	Geochemistry, 79(4), UNSP 125524 <a href="https://doi.org/10.1016/j.chemer.2019.07.006">https://doi.org/10.1016/j.chemer.2019.07.006</a>
Issue Date	2019-12
Doc URL	<a href="http://hdl.handle.net/2115/82427">http://hdl.handle.net/2115/82427</a>
Rights	© 2019. This manuscript version is made available under the CC-BY-NC-ND 4.0 license <a href="http://creativecommons.org/licenses/by-nc-nd/4.0/">http://creativecommons.org/licenses/by-nc-nd/4.0/</a>
Rights(URL)	<a href="https://creativecommons.org/licenses/by-nc-nd/4.0/">https://creativecommons.org/licenses/by-nc-nd/4.0/</a>
Type	article (author version)
File Information	Geochemistry_v79_04_1255424_.pdf



[Instructions for use](#)

1 **Heating duration of igneous rim formation on a chondrule in the Northwest Africa 3118**  
2 **CV3<sub>oxA</sub> carbonaceous chondrite inferred from micro-scale migration of the oxygen**  
3 **isotopes**

4

5 Nozomi Matsuda<sup>1\*</sup>, Naoya Sakamoto<sup>2</sup>, Shogo Tachibana<sup>1,3</sup> and Hisayoshi Yurimoto<sup>1,4</sup>

6

7 <sup>1</sup> Natural History Sciences, Hokkaido University, Sapporo 060-0810, Japan

8 <sup>2</sup> Isotope Imaging Laboratory, Creative Research Institution, Hokkaido University, Sapporo  
9 001-0021, Japan

10 <sup>3</sup> UTokyo Organization for Planetary and Space Science (UTOPS), University of Tokyo, Tokyo  
11 113-0033, Japan

12 <sup>4</sup> ISAS/JAXA, Sagami-hara, Kanagawa, 252-210, Japan

13 \*e-mail address of the corresponding author: nozomi@ep.sci.hokudai.ac.jp

14

15 **Abstract**

16 Due to their common occurrences in various types of chondrites, igneous rims formed on  
17 pre-existing chondrules throughout chondrule-forming regions of the solar nebula. Although  
18 the peak temperatures are thought to reach similar values to those achieved during chondrule  
19 formation events, the heating duration in chondrule rim formation has not been well defined.  
20 We determined the two-dimensional chemical and oxygen isotopic distributions in an igneous  
21 rim of a chondrule within the Northwest Africa 3118 CV3<sub>oxA</sub> chondrite with sub-micrometer  
22 resolution using secondary ion mass spectrometry and scanning electron microscopy. The  
23 igneous rim experienced aqueous alteration on the CV parent body. The aqueous alteration  
24 resulted in precipitation of the secondary FeO-rich olivine (Fa<sub>40-49</sub>) and slightly disturbed the  
25 Fe-Mg distribution in the MgO-rich olivine phenocrysts (Fa<sub>11-22</sub>) at about a 1  $\mu\text{m}$  scale.  
26 However, no oxygen isotopic disturbances were observed at a scale greater than 100 nm. The  
27 MgO-rich olivine, a primary phase of igneous rim formation, has  $\delta^{17}\text{O} = -6\pm 3\text{‰}$  and  $\delta^{18}\text{O} =$   
28  $-1\pm 4\text{‰}$ , and some grains contain extreme  $^{16}\text{O}$ -rich areas ( $\delta^{17}\text{O}, \delta^{18}\text{O} = \sim -30\text{‰}$ ) nearly 10  $\mu\text{m}$   
29 across. We detected oxygen isotopic migration of approximately 1  $\mu\text{m}$  at the boundaries of the  
30 extreme  $^{16}\text{O}$ -rich areas. Using oxygen self-diffusivity in olivine, the heating time of the  
31 igneous rim formation could have continued from several hours to several days at near  
32 liquidus temperatures ( $\sim 2000\text{ K}$ ) in the solar nebula suggesting that the rim formed by a  
33 similar flash heating event that formed the chondrules.

34

## 35 1. INTRODUCTION

36 It is believed that chondrules formed during flash heating events in the solar nebula  
37 (e.g., Gooding et al., 1980; Grossman and Wasson, 1982; Hewins, 1996). Chondrules are often  
38 surrounded by rims that formed in the nebula after the host chondrules. Chondrule rims are  
39 divided into two types: (1) fine-grained or matrix-like rims that are similar in chemical  
40 composition and grain size to the host chondrite matrix (e.g., Ashworth, 1977; Allen et al.,  
41 1980; King and King, 1981; Scott et al., 1984), and (2) coarse-grained or igneous rims that  
42 show evidence of a high degree of melting (e.g., Rubin, 1984; Rubin and Wasson, 1987; Krot  
43 and Wasson, 1995). Igneous rims surround ~50%, ~10% and <1% of chondrules in the CV3,  
44 H-L-LL3, and CO3 chondrites, respectively (Rubin, 1984). The ubiquitous occurrence of  
45 igneous rims across the chondrite groups suggests that igneous rim formation commonly  
46 occurred in the solar nebula and was related to chondrule formation. However, the rim  
47 formation process is not as well understood compared with chondrule formation. For example,  
48 even the heating duration has not yet been evaluated.

49 Olivine phenocrysts within igneous rims sometimes contain very <sup>16</sup>O-rich areas in  
50 their interiors (e.g., Takeda et al., 2002; Nagashima et al., 2003, 2011, 2013, 2015). The  
51 <sup>16</sup>O-rich composition is clearly distinct from that of most olivine in the igneous rims and the  
52 phenocrysts in the host chondrules, and is similar to that of amoeboid olivine aggregates. Such  
53 <sup>16</sup>O-rich olivine cannot form during chondrule formation because the oxygen isotopic  
54 compositions of the minerals crystallized from chondrule melts are typically close to those of  
55 the rocky planets (Yurimoto et al., 2008; Tenner et al., 2018). Therefore, these <sup>16</sup>O-rich  
56 olivines are the igneous rim feedstocks and heating process survivors (i.e. relict grain) from  
57 the igneous rim formation, and the rim formation process could be traced using these olivines.

58 To constrain the rim formation process, we studied the two-dimensional  
59 micro-distribution of the chemical compositions and oxygen isotopes in an igneous rim from  
60 the Northwest Africa (NWA) 3118 CV<sub>oxA</sub> chondrite intercorrelated with petrography.

61

## 62 2. ANALYTICAL TECHNIQUES

### 63 2.1. Petrography and X-ray analysis

64 A polished thin section sample of the NWA 3118 CV<sub>oxA</sub> chondrite containing an  
65 igneous rimmed porphyritic olivine chondrule was used in this study. The section was coated  
66 with a thin film (~20 nm) of carbon for the petrographic observations, quantitative elemental  
67 analysis, and X-ray elemental mapping using a field emission scanning electron microscope  
68 (FE-SEM; JEOL JSM-7000F) equipped with an energy dispersive spectrometer (EDS;  
69 Oxford X-Max 150) at the Hokkaido University. In addition, a crystallographic orientation  
70 map was obtained using an electron backscattered diffraction (EBSD; Oxford HKL)

71 installed on the FE-SEM. A 15 keV electron beam probe was applied with currents of 0.3 nA  
72 and 5 nA for the quantitative chemical analysis, and X-ray elemental mapping and EBSD  
73 mapping, respectively. The step sizes and the dwell times for the mapping were typically set  
74 at 0.5  $\mu\text{m}$  and 10  $\mu\text{s}$ , respectively.

75

## 76 **2.2. SIMS point analysis for O isotopic composition**

77 The section was coated with a Au thin film (70 nm) before the secondary ion  
78 mass spectrometry (SIMS) analysis. The point analyses of oxygen isotopes were made using  
79 a SIMS (Cameca ims-1280HR) at Hokkaido University. We applied a focused  $\text{Cs}^+$  ion  
80 primary beam (3–5  $\mu\text{m}$  in diameter) with a total kinetic energy of 20 keV. A normal incident  
81 electron gun was used for charge compensation on the primary beam irradiated area. The  
82 secondary ions of  $^{16}\text{O}^-$  sputtered by the primary beam were accelerated to 10 keV and  
83 measured using a Faraday cup (FC), and the  $^{17}\text{O}^-$  and  $^{18}\text{O}^-$  were measured using an electron  
84 multiplier (EM) in the peak jumping mode of the sector magnet. The mass resolution power  
85 (MRP) of  $M/\Delta M$  was set at  $\sim 5500$  to ensure that the contribution of  $^{16}\text{OH}^-$  to  $^{17}\text{O}^-$  was  
86 negligible. The  $^{16}\text{O}^-$  signals were obtained by subtracting background counts of the FC from  
87 the total FC counts of  $^{16}\text{O}^-$ . The EM was operated in the pulse counting mode with a dead  
88 time of 48 ns. A typical count rate for  $^{16}\text{O}^-$  was set as  $\sim 8 \times 10^7$  cps. Each measurement was  
89 conducted for 30 cycles of a counting sequence with  $^{16}\text{O}^-$  for 1 s,  $^{17}\text{O}^-$  for 2 s, and  $^{18}\text{O}^-$  for 1  
90 s with a waiting time of 2 s for every mass to stabilize the sector magnetic field. The  
91 instrumental mass fractionation was corrected using an olivine crystal from San Carlos,  
92 Arizona, USA ( $\text{Fa}_8$ ,  $\delta^{17}\text{O}_{\text{SMOW}} = 2.7\%$ ,  $\delta^{18}\text{O}_{\text{SMOW}} = 5.2\%$ ; Yurimoto et al., 2011).

93

## 94 **2.3. Isotopography for O isotopic composition**

95 The quantitative oxygen isotope distribution (isotopography) on the thin section  
96 was performed using an isotope microscope system (Cameca ims-1270 + SCAPS) at the  
97 Hokkaido University (Yurimoto et al., 2003). A static  $\text{Cs}^+$  primary beam of 20 keV was  
98 homogeneously irradiated on the sample area with an oval shape approximately 70  $\mu\text{m}$  in  
99 diameter with a beam current of  $\sim 0.5$ –2 nA. A normal incident electron gun was utilized to  
100 compensate positive charging of the sputtered region due to the primary beam irradiation. An  
101 accelerating voltage of 10 kV was applied and secondary ions of 10 keV  $\pm 75$  eV were  
102 measured by a stacked CMOS-type active pixel sensor (SCAPS) using the energy band-pass  
103 slit in the ims-1270. A contrast aperture of 150  $\mu\text{m}$  in diameter was used. The exit slit was  
104 narrowed enough to eliminate the contribution of interference ions to the isotope images. The  
105 isotope image was projected on the SCAPS detector that has  $600 \times 576$  pixels with a stacked  
106 electrode for each pixel and directly detects the secondary ions (Takayanagi et al., 2003). Each

107 pixel can store the signal of up to 50,000 ions and the pixel size corresponds to 0.28  $\mu\text{m}$  of the  
108 isotope image. The stored charge in the capacitor of a pixel can be read out individually  
109 through a readout transistor without destruction of the charge and an operating reset transistor  
110 (a non-destructive readout mode). This function realizes the SCAPS detector as an  
111 integral-type ion detector. The charge signal was acquired with the PXI system controlled by  
112 LabVIEW software (Sakamoto and Yurimoto, 2006). The readout time for one image frame  
113 was 5.25 s with a noise level of 55  $\mu\text{V}$  corresponding to 1.8 ions in the non-destructive readout  
114 mode (Yamamoto et al., 2010). The typical mass sequence for acquiring the secondary ion  
115 images for one cycle was ‘reset’,  $^{27}\text{Al}^{16}\text{O}^-$ ,  $^{56}\text{Fe}^{16}\text{O}^-$ ,  $^{24}\text{Mg}^{16}\text{O}^-$ ,  $^{28}\text{Si}^-$ , ‘reset’,  $^{16}\text{O}^-$ , ‘reset’,  $^{18}\text{O}^-$   
116 and  $^{16}\text{O}^-$ . The ‘reset’ images were taken during the resetting operation of the pixel capacitors  
117 (a destructive readout mode) and used as the reset frames for the fixed pattern noise correction  
118 (Matsumoto et al., 1993; Kunihiro et al., 2001; Nagashima et al., 2001; Takayanagi et al.,  
119 2003). The typical measurement times for the secondary ion species during one cycle were 420  
120 s for reset, 25 s for  $^{27}\text{Al}^{16}\text{O}^-$ , 50 s for  $^{56}\text{Fe}^{16}\text{O}^-$ , 50 s for  $^{24}\text{Mg}^{16}\text{O}^-$ , 10 s for  $^{28}\text{Si}^-$ , 420 s for reset,  
121 5 s for  $^{16}\text{O}^-$ , 420 s for reset, 250 s for  $^{18}\text{O}^-$ , and 5 s for  $^{16}\text{O}^-$ . Each isotopograph was calibrated  
122 in the non-destructive readout mode. The last part of the analytical cycle (‘reset’,  $^{18}\text{O}^-$  and  
123  $^{16}\text{O}^-$ ) was repeated several times in order to integrate the secondary ion signals to improve the  
124 precisions of isotopograph. The acquired  $^{16}\text{O}^-$  and  $^{18}\text{O}^-$  isotopographs were averaged for each  
125 isotope after an image shift correction (Sakamoto et al., 2007; Park et al., 2012). The amount  
126 of image shift was 1 to 3 pixels corresponding to 0.28 to 0.84  $\mu\text{m}$  on the sample surface. The  
127  $\delta^{18}\text{O}$  isotopographs were obtained by calculating secondary ion ratios of the  $^{18}\text{O}/^{16}\text{O}$  and  
128 normalized to the SMOW scale using  $\delta^{18}\text{O}$  values of minerals obtained by point analyses. The  
129 typical precision ( $2S$ ) of the  $\delta^{18}\text{O}$  isotopographs is 30‰ per pixel corresponding to 0.28  $\mu\text{m}$   
130  $\times$  0.28  $\mu\text{m}$  on the isotope image. An image processing method of moving average with  $3 \times 3$   
131 pixels was applied to the isotope ratio images to reduce the statistical fluctuation of the  
132 secondary ions. Therefore, the precision of the isotope ratio is improved to  $\sim 10$ ‰ per pixel for  
133 the smoothed image. The  $\delta^{18}\text{O}$  values of the olivine grains in the isotopography were  
134 calculated from an  $11 \times 11$  pixels area that corresponds to the beam spot size (approximately  $3$   
135  $\times 3 \mu\text{m}^2$ ) for the spot analysis. The spatial resolution of the isotopography is evaluated by the  
136 boundaries between the extremely  $^{16}\text{O}$ -rich olivine and the FeO-rich olivine that is defined by  
137 the width between 16% and 84% of the oxygen isotopic composition difference across the  
138 boundary (Fig. 1). The spatial resolution of the  $\delta^{18}\text{O}$  isotopograph is calculated to be 0.8  $\mu\text{m}$ .

139

### 140 3. RESULTS

#### 141 3.1. Petrography and mineralogy

##### 142 3.1.1. Chondrule

143 The Northwest Africa (NWA) 3118 is the oxidized Allende-like CV3<sub>oxA</sub>  
144 carbonaceous chondrite (Russell et al., 2005). The chondrule studied is completely surrounded  
145 by a coarse-grained igneous rim (Fig. 2a). The chondrule has a rounded shape of 1.4 mm  
146 diameter with a type I (Mg# (= molar MgO/(MgO + FeO) %)  $\geq$  90)) porphyritic texture. The  
147 chondrule is mainly composed of olivine phenocrysts (Fa<sub>2-5</sub>) and mesostasis in addition to  
148 opaque nodules. The major elemental compositions of these phases are listed in Tables S1–S3  
149 (Figs. S1–S3).

150 The olivine phenocrysts are euhedral and have a core-mantle structure. The grain  
151 shapes and sizes are rounded and smaller (20–150  $\mu$ m) in the core, and an elliptic and larger  
152 (200–300  $\mu$ m) in the mantle. The mesostasis of the chondrule is represented by dendritic  
153 plagioclase and augite (Fig. S4). The plagioclase is often replaced by nepheline, a secondary  
154 mineral formed during parent-body aqueous alteration and metamorphism. The secondary  
155 nepheline is abundant on the periphery (Figs. 2b, c). Opaque phases occur as rounded to  
156 sub-rounded nodules consisting of Fe-Ni metal, Fe sulfide, and metal-sulfide aggregates (Fig.  
157 S5). The Fe-Ni metal and Fe sulfide are often replaced by magnetite.

158

### 159 3.1.2. Igneous rim

160 A coarse-grained igneous rim with thickness up to 400  $\mu$ m occurs continuously  
161 around the chondrule (Fig. 2a). Mechanical cracks occur near the boundary between the  
162 chondrule and the coarse-grained rim. The cracks are secondary in origin, formed after the  
163 formation of the rim because the cracked olivine-grains show the same crystallographic  
164 orientations across the cracks, indicating that they were originally single crystal grains (Figs.  
165 S6a, b).

166 The coarse-grained rim is dominated by olivine. The olivine grains are enriched  
167 in FeO compared with those within the host chondrule. The FeO contents show a bimodal  
168 distribution with peaks at MgO-rich (Fa<sub>~11-22</sub>) and FeO-rich (Fa<sub>~40-49</sub>) compositions (Figs. S7,  
169 S8 and Table S4). Enstatite, pigeonite, feldspathic glasses, augite, nepheline, and Fe $\pm$ Ni  
170 sulfide (troilite, pyrrhotite or pentlandite) are identified in the rim (Fig. S6a). The major  
171 elemental compositions of these minerals are summarized in Tables S5–S8 (Figs. S9 and  
172 S10).

173 Enstatite and pigeonite (Fs<sub>1-4</sub>Wo<sub>1-2</sub> and Fs<sub>1-4</sub>Wo<sub>4-10</sub>) are subhedral and often  
174 partially replaced by FeO-rich olivine (Fig. S11a). Augite (Fs<sub>1-5</sub>Wo<sub>27-42</sub>) overgrows on the  
175 enstatite and pigeonite, (Fig. S11a) and occurs in the mesostasis of the rim. The rim contains  
176 abundant spherical or irregular assemblages of Fe- and Fe-Ni sulfides (troilite, pyrrhotite,  
177 and pentlandite), whereas Fe-Ni metal and magnetite are rare (Fig. S11b). They are also  
178 replaced by FeO-rich olivine (Fig. S11c). Feldspathic glass and nepheline occur in the

179 mesostasis (Fig. S11a). These petrographic observations are similar to those reported in the  
180 Allende meteorite by Brearley and Krot (2013), who showed that aqueous alteration took  
181 place on the parent body.

182         The MgO-rich olivine grains are euhedral to subhedral. Their grain size gradually  
183 changes radially from 100–150  $\mu\text{m}$  near the chondrule-rim boundary to 10–50  $\mu\text{m}$  at the  
184 rim-matrix boundary (Figs. S6a, b). Some MgO-rich olivine grains are overgrown by  
185 FeO-rich olivine with the same crystallographic orientation (Figs. 3a, c). The cracks of the  
186 MgO-rich olivine grains are healed by FeO-rich olivine as veins (Figs. 3b, d).

187         The FeO-rich olivine appears anhedral and fills the spaces among the other  
188 minerals in the rim (Fig. S11a). The compositions of FeO-rich olivine gradually change from  
189  $\text{Fa}_{42}$  at the chondrule-rim boundary to  $\text{Fa}_{48}$  at the rim-matrix boundary (Fig. S12). The  
190 igneous rim is covered with FeO-rich olivine at the matrix-rim boundary (Fig. S13a). The  
191 FeO-rich olivines show both smooth and porous surfaces on the polished thin section (Fig.  
192 S13b).

193         The MgO-rich olivine grains in the igneous rim have Fe-Mg chemical zoning near  
194 ~~many~~ crystal surfaces. Where there are grains with FeO-rich olivine overgrowths, the zoning  
195 gradients occur perpendicular to the surfaces of the MgO-rich olivine (Figs. 4a–f). No  
196 Mg-Fe zoning is observed ~~within the mantling~~ on the sides of the FeO-rich olivines.  
197 Gradients in Mg-Fe composition also occur perpendicular to the veins in the MgO-rich  
198 olivine grains (Figs. 4g–h).

199

### 200 3.1.3 Matrix

201         The matrix surrounding the igneous rim is predominantly composed of olivine with  
202  $\text{Fa}_{46-51}$ . The olivine composition is similar to the FeO-rich olivine in the igneous rim (Table.  
203 S9). The olivine grains show a bimodal size distribution; the coarser-grains (5–10  $\mu\text{m}$ ) are  
204 either needle-shaped or irregular; the finer-grains (< 1 $\mu\text{m}$ ) are needle-shaped (Fig. S14a).  
205 Neither fayalite (>  $\text{Fa}_{90}$ ) nor phyllosilicates are observed. Sulfides and Ca, Fe-rich silicates are  
206 scattered throughout the matrix (Fig. S14b).

207

## 208 3.2. Oxygen-isotope distribution of olivine

### 209 3.2.1 Chondrule and igneous rim

210         On the oxygen three-isotope diagram ( $\delta^{17}\text{O}$  vs.  $\delta^{18}\text{O}$ ), the compositions of olivine  
211 phenocrysts in the host chondrule measured by the point analyses plot on a  $\sim$  slope-1 line  
212 (CCAM) ( $\delta^{17}\text{O} = -7.6 \pm 2.1\%$ ,  $\delta^{18}\text{O} = -3.8 \pm 2.1\%$ ,  $2\sigma$ ; Fig. 5 and Table S10). The oxygen  
213 isotopic compositions of olivines in the igneous rim that are also obtained by point analyses  
214 are distributed heterogeneously along the  $\sim$  slope-1 line (Fig. 5, Table S11 and Fig. S15). The

215 oxygen isotopic compositions of the FeO-rich olivines are  $^{16}\text{O}$ -poor ( $\delta^{17}\text{O} = 2.0 \pm 1.8\text{‰}$ ,  $\delta^{18}\text{O}$   
216  $= 8.1 \pm 3.6\text{‰}$  on average). In contrast, the MgO-rich olivine grains are relatively  $^{16}\text{O}$ -rich  
217 ( $\delta^{17}\text{O} = -5.6 \pm 3.2\text{‰}$ ,  $\delta^{18}\text{O} = -0.7 \pm 3.6\text{‰}$  on average). The standard deviations for  $\delta^{17}\text{O}$  and  
218  $\delta^{18}\text{O}$  ( $2\sigma = 1.8$  and  $3.6\text{‰}$ , respectively) suggest that the O isotope variation is mass-dependent  
219 for the FeO-rich olivine, whereas the variation for MgO-rich olivine appears to be mass  
220 independent with a slope-1 variation ( $2\sigma = 3.2$  and  $3.6\text{‰}$  for  $\delta^{17}\text{O}$  and  $\delta^{18}\text{O}$ ). One distinct  
221 composition ( $\delta^{17}\text{O} = -18\text{‰}$  and  $\delta^{18}\text{O} = -15\text{‰}$ ) was observed for a MgO-rich olivine grain in  
222 the igneous rim. As discussed in the next section, this distinct composition could be a result of  
223 a primary beam overlap across areas with two different oxygen isotopic compositions in the  
224 MgO-rich olivine, i.e.,  $\delta^{17}\text{O} \sim -6\text{‰}$ ,  $\delta^{18}\text{O} \sim -1\text{‰}$  and  $\delta^{17,18}\text{O} \sim -30\text{‰}$ .

225

### 226 **3.2.2. Heterogeneous oxygen isotope distribution within the MgO-rich olivine crystals**

227 Using isotopography, we discovered that MgO-rich olivine grains in the igneous rim  
228 sometimes contain extreme  $^{16}\text{O}$ -rich areas in their interiors. The MgO-rich olivine grains  
229 containing the extreme  $^{16}\text{O}$ -rich areas tend to be present near the boundary between the  
230 igneous rim and adjacent matrix, and were not found near the rim-chondrule boundary (Fig. 6).

231 The MgO-rich olivine (about  $27\ \mu\text{m}$  in size) in the center of Figure 7a has variable  
232 intra-crystalline oxygen-isotope compositions. The oxygen isotopic compositions of MgO-rich  
233 olivine in the area that appears dark blue in Figure 7a and the surrounding white to blue area  
234 are  $\delta^{18}\text{O} = -30.6 \pm 3.7\text{‰}$  and  $-1.9 \pm 2.9\text{‰}$ , respectively. The extreme  $^{16}\text{O}$ -rich area is not  
235 chemically distinct from the surrounding MgO-rich olivine. The oxygen isotopic composition  
236 of the MgO-rich olivine surrounding the  $^{16}\text{O}$ -rich ~~patch~~ area is consistent with most of the  
237 measured point analyses (i.e., except for the one point analysis with  $\delta^{18}\text{O} = -14.5\text{‰}$ ; see Fig. 5  
238 and Table S11). The  $\delta^{18}\text{O}$  for the FeO-rich olivine is  $10.4 \pm 3.0\text{‰}$  consistent with those from  
239 point analyses. The  $^{16}\text{O}$ -rich analysis shown in Figure 5 ( $\delta^{17}\text{O} = -18\text{‰}$ ,  $\delta^{18}\text{O} = -15\text{‰}$ ; analysis  
240 number 15 in Table S11) was collected from the boundary between the extreme  $^{16}\text{O}$ -rich ~~patch~~  
241 area and the surrounding olivine (Fig. S15).

242 The olivine crystal shown in Figure 7b has two different chemical compositions; an  
243 upper MgO-rich area and a lower FeO-rich area. The MgO-rich area of the olivine includes an  
244 extreme  $^{16}\text{O}$ -rich area ( $\delta^{18}\text{O} = -16.1 \pm 3.3\text{‰}$ ). The upper side of the extreme  $^{16}\text{O}$ -rich area  
245 directly contacts the MgO-rich olivine, whereas the lower side directly contacts the overgrown  
246 FeO-rich olivine. The MgO-rich area of the olivine has Fe-Mg chemical zoning at the  
247 boundary with the FeO-rich overgrowth. The  $\delta^{18}\text{O}$  value in the upper area of the MgO-rich  
248 olivine is  $-2.3 \pm 3.4\text{‰}$ . The two different oxygen isotope areas in the MgO-rich olivine are  
249 indistinguishable in the chemical compositions. The  $\delta^{18}\text{O}$  value of the FeO-rich overgrown  
250 olivine is  $11.1 \pm 3.3\text{‰}$ .

251 The MgO-rich olivine (about 27  $\mu\text{m}$  in size;  $\delta^{18}\text{O} = -2.5 \pm 2.9\%$ ) in the center of  
252 Figure 7c includes two extreme  $^{16}\text{O}$ -rich areas. The larger area has  $\delta^{18}\text{O}$  value of  $-33.1 \pm 3.2\%$ .  
253 These two areas could be connected in three dimensions (above or below the thin section  
254 surface) because they have the same crystallographic orientation. A part of the upper boundary  
255 of the larger area is directly adjacent to the overgrown FeO-rich olivine (Fig. 1) with  $\delta^{18}\text{O}$   
256 value of  $6.5 \pm 2.6\%$ .

257 The MgO-rich olivine in the center of Figure 7d is about 26  $\mu\text{m}$  in size and partially  
258 overgrown by FeO-rich olivine. This olivine includes two extreme  $^{16}\text{O}$ -rich areas with  $\delta^{18}\text{O}$   
259 values of  $-30.2 \pm 3.4\%$  and  $-28.3 \pm 4.9\%$ , respectively. The oxygen isotopic compositions are  
260 the same within the measurement error and their crystallographic orientations are also the  
261 same. Therefore, these two areas could be one region connected above or below the thin  
262 section surface. The surrounding MgO-rich olivine area has  $\delta^{18}\text{O}$  value of  $-1.4 \pm 3.1\%$  that is  
263 typical for the MgO-rich olivine in this igneous rim. The FeO-rich olivine in Figure 7d also  
264 has the typical oxygen isotopic composition of  $\delta^{18}\text{O} = 5.9 \pm 3.2\%$ . The olivine grains adjacent  
265 to the upper right include two extreme  $^{16}\text{O}$ -rich areas with  $\delta^{18}\text{O}$  values of  $-15.4 \pm 5.1\%$   
266 (smaller area) and  $-24.0 \pm 5.0\%$  (larger area). Although the olivine grains seem to be FeO-rich,  
267 the extreme  $^{16}\text{O}$ -rich areas are slightly enriched in MgO composition according to the BSE  
268 image suggesting that the extreme  $^{16}\text{O}$ -rich areas were originally enriched in MgO. Parts of the  
269 FeO-rich olivine outside of the extreme  $^{16}\text{O}$ -rich areas have the typical oxygen isotopic  
270 composition of FeO-rich olivine in the igneous rim.

271 The MgO-rich olivine grain ( $\delta^{18}\text{O} = -4.3 \pm 2.7\%$ ) on the left side of Figure 7e is  
272 about 20  $\mu\text{m}$  in size and includes an extreme  $^{16}\text{O}$ -rich area with  $\delta^{18}\text{O}$  values of  $-19.8 \pm 3.4\%$ .  
273 The MgO-rich olivine is overgrown by FeO-rich olivine with  $\delta^{18}\text{O}$  value of  $6.2 \pm 4.0\%$ . The  
274 MgO-rich olivine grain (about 30  $\mu\text{m}$ ) on the right side ( $\delta^{18}\text{O} = -1.7 \pm 2.7\%$ ) includes an  
275 extreme  $^{16}\text{O}$ -rich area with  $\delta^{18}\text{O}$  value of  $-16.9 \pm 3.0\%$ .

276 The  $\delta^{18}\text{O}$  image in Figure 7f was normalized to the SMOW scale using the average  
277  $\delta^{18}\text{O}$  value of the MgO-rich olivine in the rim obtained by spot analyses ( $\delta^{18}\text{O} = -0.7 \pm 3.6\%$ ,  
278 Table S10) because spot analyses of oxygen isotopes were not applied in this image field. The  
279 MgO-rich olivine grain ( $\sim 35$   $\mu\text{m}$  across) is separated by a crack and includes an extreme  $\delta^{18}\text{O}$   
280 area across the crack ( $\delta^{18}\text{O} = -31.5 \pm 4.7\%$ ). The FeO-rich olivine has an oxygen isotopic  
281 composition of  $\delta^{18}\text{O} = 12.0 \pm 2.0\%$ .

282 In summary, most of the oxygen isotopic compositions of the FeO-rich and  
283 MgO-rich olivines determined by SCAPS are  $\sim 8\%$  and  $\sim -2\%$  for  $\delta^{18}\text{O}$ , respectively, for all  
284 the image fields and these values are consistent with those obtained by the SIMS spot analyses.  
285 The MgO rich olivines often include extreme  $^{16}\text{O}$ -rich areas with sizes typically less than 10  
286  $\mu\text{m}$ . The oxygen isotopic compositions of the extreme  $^{16}\text{O}$ -rich areas are typically  $\delta^{18}\text{O} \sim$

287  $-30\text{‰}$  (and  $\delta^{17}\text{O} \sim -30\text{‰}$  inferred from combining the results of the point analysis), but tends  
288 toward less  $^{16}\text{O}$ -rich values for areas having narrow boundaries ( $<3 \mu\text{m}$  across) with adjacent  
289  $^{16}\text{O}$ -poor olivine. This tendency of oxygen isotopic variation can be interpreted by the spatial  
290 resolution of isotopography of this study (Fig. 1), the oxygen self-diffusion discussed in  
291 section 4.2, and supports that the extreme  $^{16}\text{O}$ -rich areas in this igneous rim have  $\delta^{17,18}\text{O} \sim \delta^{18}\text{O}$   
292 values of  $\sim -30\text{‰}$ .

293

## 294 4. DISCUSSION

### 295 4.1. Aqueous alteration on the parent body

296 The occurrences of secondary minerals – FeO-rich olivine ( $\text{Fa}_{40-49}$ ), nepheline,  
297 magnetite, and Ca,Fe-rich silicates, and their petrographic textures observed in this study  
298 suggest that NWA3118 experienced extensive aqueous/metasomatic alteration on the CV  
299 chondrite parent body (e.g., Krot et al., 1995, 1998, 2004; Maruyama et al., 1999; Maruyama  
300 and Yurimoto, 2003; Brearley, 2003). The FeO-rich secondary olivine exhibits textures such as  
301 (1) overgrowths around individual MgO-rich olivine grains, (2) veins in the MgO-rich olivine  
302 grains, (3) replacement of enstatite and pigeonite, and opaque nodules, and (4) lath-shaped  
303 grains in the matrix, which are similar to those observed in Allende (e.g. Krot et al., 1995,  
304 1998, 2004; Komatsu et al., 2015; Cuvillier et al., 2015) suggesting origin by aqueous  
305 alteration origin on the CV parent body.

306 Chemical compositions are different between olivine grains in the igneous rim,  
307  $\text{Fa}_{11-22}$ , and in the host chondrule,  $\text{Fa}_{2-5}$ . The characteristics of  $\text{Fa}_{11-22}$  might be due to  
308 metamorphic processes on the parent body (Huss et al., 2006; Tenner et al., 2015). If the  
309  $\text{Fa}_{11-22}$  are the result of metamorphic processes on the parent body, the MgO-rich olivine in  
310 the host chondrule contacted to the  $\text{Fa}_{11-22}$  olivine also must have similar Fa composition.  
311 However, the MgO-rich olivine of the host chondrule has clearly distinct chemical  
312 composition,  $\text{Fa}_{2-5}$  and the chemical compositions of olivine are abruptly changed at the  
313 chondrule-rim boundary (Figs. S6 and S8). If the  $\text{Fa}_{11-22}$  are the result of metamorphic  
314 processes on the parent body, Fe-Mg interdiffusion should have occurred in the MgO-rich  
315 olivine. We calculated Fe-Mg interdiffusion profiles assuming that Fa composition at the  
316 center of olivine grain changed from  $\text{Fa}_2$  to  $\text{Fa}_{15}$  on the parent body. The interdiffusion profiles  
317 are inconsistent with compositional zoning in the igneous rim olivine (Fig. 4). Therefore, it is  
318 unlikely that the  $\text{Fa}_{11-22}$  composition of the MgO-rich olivines in the igneous rim was achieved  
319 by metamorphic processes on the parent body. The MgO-rich olivines with  $\text{Fa}_{11-22}$  in the  
320 igneous rim are the original composition when the igneous rim formed.

321

322 The Fe-Mg chemical zoning between the MgO-rich olivine and adjacent FeO-rich  
323 olivine in the igneous rim is an inter-diffusion profiles during the alteration on the parent body,  
324 and can be used as a probe to determine timescales and temperature of the alteration (e.g.,  
325 Weinbruch et al., 1994). We defined the Fe-Mg inter-diffusion distance from the interface  
326 ( $x_{\text{Fe-Mg}} = 0$ ) between the FeO-rich olivine (FeO content =  $C_1$ ) and MgO-rich olivine (FeO  
327 content in the core =  $C_2$ ) as the distance  $x_{\text{Fe-Mg}}$  with the FeO content of  $(C_1 - C_2)/e + C_2$  (Fig. 4,  
328 Tables S12). For example, in Figure 4a, the Fe-Mg inter-diffusion distance  $x_{\text{Fe-Mg}}$  from the  
329 FeO-rich olivine with 37 wt% FeO into the MgO-rich olivine with 21 wt% FeO is 1.3  $\mu\text{m}$ .  
330 Similarly, the Fe-Mg inter-diffusion distances shown in Figures 4b to 4f are 1.8, 1.1, 1.3, 1.3,  
331 and 2.1  $\mu\text{m}$ , respectively.

332 The diffusion distance from veins of the FeO-rich olivine was also analyzed on both  
333 sides across veins in MgO-rich olivine (Figs. 4g, h). The interface between the vein and  
334 MgO-rich olivine is defined as  $x_{\text{Fe-Mg}} = 0$ . Diffusion distances of 1.1  $\mu\text{m}$  from 27 wt% FeO to 15  
335 wt% FeO and 1.2  $\mu\text{m}$  from 28 wt% FeO to 15 wt% FeO were obtained on both sides of the vein  
336 for the grain shown in Figure 4g. Similarly, diffusion distances of 1.2 and 1.0  $\mu\text{m}$  were  
337 obtained across the vein from 31 to 21 wt% FeO and from 30 to 20 wt% FeO for the grain in  
338 Figure 4h.

339 The interdiffusion distances observed in the olivine grains range from 1.0  $\mu\text{m}$  to 2.1  
340  $\mu\text{m}$ . The longer diffusion distances shown in Figures 4b (1.8  $\mu\text{m}$ ) and 4f (2.1  $\mu\text{m}$ ) could reflect  
341 the anisotropy of Fe-Mg diffusion in olivine that is faster along the c-axis (space group: Pbnm)  
342 than along the a- or b-axis (Dohmen and Chakraborty, 2007). The Fe-Mg diffusion distance  
343 recorded within the MgO-rich olivine in the igneous rim is an average of 1.3  $\mu\text{m}$  regardless of  
344 the grain location in the igneous rim (Fig. S8). Our observations of Fe-Mg diffusion agree with  
345 those observed in the matrix olivine grains of the Allende CV<sub>oxA</sub> chondrite (Cuvillier et al.,  
346 2015).

347 The Fe-Mg interdiffusion profiles show that the concentration gradient is present  
348 only on the MgO-rich olivine side, not within the overgrown FeO-rich olivine. Cuvillier et al.  
349 (2015) proposed that the composition in the FeO-rich olivine is homogeneous because  
350 diffusion in FeO-rich olivine is faster than in MgO-rich olivine and the compositional jump  
351 derives from resistance that prevents equilibrium at the interface. They also mention that this  
352 resistance is not known to occur in olivine grains. Alternatively, the Fe-Mg interdiffusion  
353 could have mainly formed in the MgO-rich olivine with dissolved Fe ions in a  
354 high-temperature aqueous fluid before ~~or during~~ precipitation of FeO-rich olivine. The  
355 FeO-rich olivine may have precipitated interstitially on the MgO-rich olivine and the  
356 intergranular spaces between minerals in the igneous rim after cooling. Fe-Mg diffusion

357 profiles in the Fe-rich olivines, thus, were not appeared due to the slow diffusivity at the low  
358 temperature.

359 The diffusion distances for the Fe-Mg interdiffusion,  $x_{\text{Fe-Mg}}$ , and O self-diffusion,  
360  $x_{\text{oxygen}}$ , are approximated as:

$$361 \quad x_{\text{Fe-Mg}} = \sqrt{2D_{\text{Fe-Mg}} t} \quad (1)$$

$$362 \quad x_{\text{oxygen}} = \sqrt{2D_{\text{oxygen}} t} \quad (2)$$

363 where  $D$  is the diffusion coefficient for the corresponding species and  $t$  is the time. We ignore  
364 the compositional dependence of  $D_{\text{Fe-Mg}}$  for simplicity. If these diffusion processes occurred  
365 simultaneously in the olivine of the igneous rim, the diffusion distances should be correlated as  
366 follows;

$$367 \quad x_{\text{oxygen}} = x_{\text{Fe-Mg}} \sqrt{\frac{D_{\text{oxygen}}}{D_{\text{Fe-Mg}}}} \quad (3)$$

368 The average  $x_{\text{Fe-Mg}}$  is 1.3  $\mu\text{m}$  in this study and  $x_{\text{oxygen}}$  is then given as a function of  
369 temperature independently from the diffusion time (duration of aqueous alteration). The  
370 Fe-Mg inter-diffusion and oxygen self-diffusion coefficients in olivine have been measured in  
371 several previous studies. Nakamura and Schmalzried (1984) determined the Fe-Mg  
372 inter-diffusion coefficient ( $D_{\text{N\&S}}$ ) at temperatures between 1323 and 1553 K and a composition  
373 of Fo<sub>87</sub>. Chacraborty (1997) also reported the Fe-Mg inter-diffusion coefficient ( $D_{\text{C}}$ ) at  
374 temperatures between 1253 and 1573 K and a composition of Fo<sub>86</sub>. Their diffusion coefficients  
375 were obtained under a controlled oxygen fugacity of  $f\text{O}_2 = 10^{-12}$  bars. Dohmen et al. (2007)  
376 determined the Fe-Mg interdiffusion coefficients of Fo<sub>86</sub> at temperatures from 973–1473 K.  
377 The diffusion coefficients were obtained at  $f\text{O}_2$  of  $10^{-12}$  bars at temperatures between  
378 1173–1473 K ( $D_{\text{D\_hightemp}}$ ), while those between 973–1123 K were obtained at  $f\text{O}_2$  of  
379  $10^{-15}$ - $10^{-17}$  bars ( $D_{\text{D\_lowtemp}}$ ). The forsterite content of the MgO-rich olivine in the igneous rim  
380 is adequate to choose these Fe-Mg interdiffusion coefficients in previous studies. However,  
381 they need to be extrapolated to lower temperatures because they were determined at  
382 temperatures higher than peak metamorphic temperatures inferred for Allende (e.g., Keil,  
383 2000; Ito and Messenger, 2010) and were extrapolated down to 500 K in this study. The  
384 Fe-Mg inter-diffusion coefficients ( $\text{m}^2/\text{s}$ ),  $D_{\text{N\&S}}$  (Nakamura and Schmaizried, 1984),  $D_{\text{C}}$   
385 (Chakraborty et al., 1997),  $D_{\text{D\_hightemp}}$  (Dohmen et al., 2007), and  $D_{\text{D\_lowtemp}}$  (Dohmen et al.,  
386 2007) were expressed as follows:

$$387 \quad D_{\text{N\&S}} = 8.33 \times 10^{-10} \cdot \exp\left[\frac{-188000}{RT}\right] \quad (4)$$

388 
$$D_C = 5.38 \times 10^{-9} \cdot \exp\left[\frac{-226000}{RT}\right] \quad (5)$$

389 
$$D_{D\_hightemp} = 6.66 \times 10^{-10} \cdot \exp\left[\frac{-201000}{RT}\right] \quad (6)$$

390 
$$D_{D\_lowtemp} = 1.54 \times 10^{-9} \cdot \exp\left[\frac{-223000}{RT}\right] \quad (7)$$

391 where  $T$  is the temperature (K) and  $R$  is the gas constant (8.314 J/mol·K).

392 The oxygen fugacity,  $fO_2$ , for the CV chondrites was estimated to be close to the  
 393 iron-wustite (IW) oxygen buffer during chondrule formation and close to the  
 394 fayalite-magnetite-quartz (FMQ) buffer during aqueous alteration (Righter and Neff, 2007).  
 395 We assumed that the diffusion occurred under the FMQ buffer during aqueous alteration that is  
 396 expressed as follows (Myers and Eugster, 1983);

397 
$$\log fO_2 = -\frac{24441.9}{T} + 8.290 \quad (8)$$

398 The  $fO_2$  corrections for  $D_{N\&S}$ ,  $D_C$ , and  $D_{D\_hightemp}$  to the FMQ were performed assuming that  
 399 the Fe-Mg interdiffusion is controlled by the vacancy concentration determined by the  $Fe^{2+}$ -  
 400  $Fe^{3+}$  equilibrium in olivine (e.g., Chakraborty et al., 1997). The  $fO_2$  corrected expressions for  
 401  $D_{Fe-Mg}$  are given as follows:

402 
$$D_{N\&S} = \left(\frac{fO_{2\_FMQ}}{fO_{2\_Ex}}\right)^{\frac{1}{6}} \cdot 8.33 \times 10^{-10} \cdot \exp\left[\frac{-188000}{RT}\right] \quad (9)$$

403 
$$D_C = \left(\frac{fO_{2\_FMQ}}{fO_{2\_Ex}}\right)^{\frac{1}{6}} \cdot 5.38 \times 10^{-9} \cdot \exp\left[\frac{-226000}{RT}\right] \quad (10)$$

404 
$$D_{D\_hightemp} = \left(\frac{fO_{2\_FMQ}}{fO_{2\_Ex}}\right)^{\frac{1}{6}} \cdot 6.66 \times 10^{-10} \cdot \exp\left[\frac{-201000}{RT}\right] \quad (11)$$

405 where  $fO_{2\_FMQ}$  is the oxygen fugacity at the FMQ buffer and  $fO_{2\_Ex}$  is that in the  
 406 experiments. Dohmen et al. (2007) reported that Fe-Mg interdiffusion at low temperatures  
 407 (below 1173 K) are independent of  $fO_2$ , most likely due to a change in the diffusion  
 408 mechanism where the vacancy concentration is controlled extrinsically by the impurity ions.  
 409 Thus, the  $fO_2$  correction was not made for  $D_{D\_lowtemp}$ .

410 The oxygen self-diffusion coefficients (m<sup>2</sup>/s) in olivine,  $D_{J\_1980}$  (Jaoul et al., 1980),  
 411  $D_{Re}$  (Reddy et al., 1980),  $D_{J\_1983}$  (Jaoul et al., 1983),  $D_{O\&A}$  (Oishi and Ando, 1984; Ando et al.,  
 412 1981),  $D_A$  (Andresson et al., 1989),  $D_{G\&J}$  (Gérard and Jaoul, 1989),  $D_{Ry}$  (Ryerson et al., 1989)  
 413 and  $D_{D\_2002}$  (Dohmen et al., 2002) are expressed as follows:

414 
$$D_{J\_1980} = 1.46 \times 10^{-8} \cdot \exp\left[\frac{-328000}{RT}\right] \quad (12)$$

415 
$$D_{\text{Re}} = 3.50 \times 10^{-7} \cdot \exp\left[\frac{-372000}{RT}\right] \quad (13)$$

416 
$$D_{\text{L}_{1983}} = 2.30 \times 10^{-10} \cdot \exp\left[\frac{-293000}{RT}\right] \quad (14)$$

417 
$$D_{\text{O\&A}} = 2.85 \times 10^{-6} \cdot \exp\left[\frac{-416000}{RT}\right] \quad (15)$$

418 
$$D_{\text{A}} = 6.86 \times 10^{-10} \cdot \exp\left[\frac{-302000}{RT}\right] \quad (16)$$

419 
$$D_{\text{G\&J}} = 6.7 \times 10^{-6} \cdot (fO_2_{\text{FMQ}})^{0.34} \cdot \exp\left[\frac{-38000}{T}\right] \quad (17)$$

420 
$$D_{\text{Ry}} = 2.6 \times 10^{-10} \cdot (fO_2_{\text{FMQ}})^{0.21} \cdot \exp\left[\frac{-226000}{RT}\right] \quad (18)$$

421 
$$D_{\text{D}_{2002}} = 4.57 \times 10^{-9} \cdot \exp\left[\frac{-338000}{RT}\right] \quad (19)$$

422 The diffusivities given by Eqs. (12–16) are independent of  $fO_2$  because they were  
 423 determined for pure forsterite, and the oxygen fugacity dependence was not determined for  
 424  $D_{\text{D}_{2002}}$ . We applied all the combinations of  $D_{\text{Fe-Mg}}$  given by Eqs. (7) and (9–11) and  $D_{\text{oxygen}}$   
 425 given by Eqs. (12–19) to Eq. (3) to calculate the possible range of  $x_{\text{oxygen}}$  for a given  $x_{\text{Fe-Mg}}$  of  
 426 1.3  $\mu\text{m}$ .

427 Figure 8 shows the change of  $x_{\text{oxygen}}$  with temperature. The  $x_{\text{oxygen}}$  is widespread over  
 428 the range from  $10^{-7}$  nm to 0.1  $\mu\text{m}$  at temperatures below 1000 K. Because the parent body of  
 429 the CV<sub>oxA</sub> chondrite was not heated above 1000 K (e.g., Keil, 2000; Ito and Messenger, 2010),  
 430  $x_{\text{oxygen}}$  should be smaller than 0.1  $\mu\text{m}$ . Therefore, the oxygen isotopic compositions in the  
 431 olivine of NWA3118 should not have been disturbed on the parent body except for a very thin  
 432 layer ( $< 0.1 \mu\text{m}$ ) of the grain boundary. Because the thickness of the possible oxygen diffusion  
 433 layer is much smaller than the spatial resolution of the oxygen isotopography (Fig. 1), the thin  
 434 layer was not observed in this study.

435

#### 436 4.2. Oxygen diffusion in MgO-rich olivine

437 Figure 9 shows the  $\delta^{18}\text{O}$  profiles at the edge of the extreme  $^{16}\text{O}$ -rich area in a  
 438 MgO-rich olivine single crystal within the igneous rim. The sharpness of the boundary defined  
 439 by  $2\sigma$ , a width between 16% and 84% of the compositional difference, is 1.5–2.3  $\mu\text{m}$ . This  
 440 value is larger than the spatial resolution of the isotopography (0.8  $\mu\text{m}$ , Fig. 1). This indicates  
 441 that oxygen isotope self-diffusion ( $\sim 1 \mu\text{m}$ ) occurred in the MgO-rich olivine across the  
 442 boundary between the different oxygen isotopic compositions prior to the parent body  
 443 accretion. The oxygen isotope self-diffusion distance of  $\sim 1 \mu\text{m}$  may also explain the

444 observation that the oxygen isotopic compositions in the extreme  $^{16}\text{O}$ -rich areas tend toward  
 445  $^{16}\text{O}$ -depletion when the area is smaller than  $3\ \mu\text{m}$  across the short side (Fig. 7).

446 Because the MgO-rich olivine of the igneous rim was crystallized from a melt  
 447 and the extreme  $^{16}\text{O}$ -rich areas in the MgO-rich olivine should have been relict crystals in  
 448 the melt, oxygen isotope exchanges in the  $^{16}\text{O}$ -rich areas should have principally occurred  
 449 during the igneous rim formation through oxygen self-diffusion in the MgO-rich olivine. We  
 450 note that forsterite dissolution occurred during the igneous-rim formation from the irregular  
 451 shapes of extreme  $^{16}\text{O}$ -rich areas and forsterite dissolution in chondrule-like melts is a very  
 452 fast process (Soulié et al. 2017). This suggests that forsterite dissolution might not have a  
 453 significant effect for the oxygen isotope self-diffusion.

454 Because the  $f\text{O}_2$  during chondrule formation was estimated to be close to the  
 455 iron-wustite (IW) oxygen buffer (Righeter and Neff, 2007), we assumed that the diffusion  
 456 occurred under the IW buffer (IW~0) as follows (Myers and Eugster, 1983);

$$457 \quad \log f\text{O}_2 = -\frac{26834.7}{T} + 6.471 \quad (20)$$

458 We note that chondrule formed under the oxygen fugacity was one or two log units below  
 459 IW (IW-1–IW-2) (Grossman et al., 2012). This difference in  $f\text{O}_2$  has no influence on our  
 460 calculation, even if  $f\text{O}_2$  is 2 orders of magnitude (IW-2) lower than our assumption (IW~0).  
 461 Because our data were normalized to an  $f\text{O}_2$  using an exponent of 1/6 for  $f\text{O}_2$  dependence of  
 462 Fe-Mg inter-diffusion in olivine (Dohmen et al., 2007). That is, only an exponent of 1/6  
 463 difference affects a diffusion coefficient. Furthermore, the Fe-Mg diffusion distance is also  
 464 proportional to the square root of a diffusion coefficient, indicating the effect of oxygen  
 465 fugacity difference is not significantly large. The  $D_{\text{Fe-Mg}}$  corrected to the IW  $f\text{O}_2$  are  
 466 expressed as follows:

$$467 \quad D_{N\&S} = \left(\frac{f\text{O}_{2\_IW}}{f\text{O}_{2\_Ex}}\right)^{\frac{1}{6}} \cdot 8.33 \times 10^{-10} \cdot \exp\left[\frac{-188000}{RT}\right] \quad (21)$$

$$468 \quad D_C = \left(\frac{f\text{O}_{2\_IW}}{f\text{O}_{2\_Ex}}\right)^{\frac{1}{6}} \cdot 5.38 \times 10^{-9} \cdot \exp\left[\frac{-226000}{RT}\right] \quad (22)$$

$$469 \quad D_{D\_hightemp} = \left(\frac{f\text{O}_{2\_IW}}{f\text{O}_{2\_Ex}}\right)^{\frac{1}{6}} \cdot 6.66 \times 10^{-10} \cdot \exp\left[\frac{-201000}{RT}\right] \quad (23)$$

470 The  $f\text{O}_{2\_IW}$  in the equations is the oxygen fugacity at the IW buffer and the  $f\text{O}_{2\_Ex}$  is the  
 471 oxygen fugacity in the experiment described above (see details in section 4.1).

472 The Fe-Mg interdiffusion coefficients in olivine at high temperatures (1673–1873  
 473 K) were also determined by Tachibana et al. (2013). The diffusion coefficient was obtained  
 474 under a controlled  $f\text{O}_2$  of  $10^{-7.5}$  bars and  $\text{Fo}_{95}$  composition:

475 
$$D_T = 4.84 \times 10^{-5} \cdot \exp\left[\frac{-323000}{RT}\right] \quad (24)$$

476 The diffusion coefficient ( $m^2/s$ ) after the  $fO_2$  correction to IW is given by:

477 
$$D_T = \left(\frac{fO_{2-IW}}{fO_{2-Ex}}\right)^{\frac{1}{6}} \cdot 4.84 \times 10^{-5} \cdot \exp\left[\frac{-323000}{RT}\right] \quad (25)$$

478 We calculated the  $x_{Fe-Mg}$  in olivine for  $x_{oxygen} = 1 \mu m$  using Eq. (3). The  $x_{Fe-Mg}$   
 479 decreases with increasing temperature (Fig. 10) and is estimated to be larger than  $10 \mu m$  for  
 480 all the combinations of  $D_{Fe-Mg}$  and  $D_{oxygen}$  up to 2000 K that is an inferred peak temperature  
 481 of chondrule formation (e.g., Hewins and Connolly, 1996; Hewins et al., 2005).

482 Because the size of the extreme  $^{16}O$ -rich areas in this study were less than  $10 \mu m$   
 483 across (Fig. 7), the calculated  $x_{Fe-Mg}$  is large enough to homogenize the Fe-Mg distribution  
 484 between the  $^{16}O$ -rich areas and the surrounding overgrown MgO-rich olivine. This is  
 485 consistent with the observations of the homogeneous chemical compositions of the  
 486 MgO-rich olivines with different oxygen isotopic compositions.

487 The heating duration for  $x_{oxygen} = 1 \mu m$  within the MgO-rich olivine in the  
 488 igneous rim was calculated to be from several hours to several days at near liquidus  
 489 temperature (2000 K) and longer than one year at near solidus temperature (1400 K) (Fig.  
 490 11). The estimated heating duration was similar to those for chondrule formation at near  
 491 liquidus temperature that was molten for up to several tens of hours (e.g., Hewins and  
 492 Connolly, 1996; Hewins et al., 2005) suggesting that the igneous rim was also formed during  
 493 transient heating events.

494

## 495 5. Conclusions

496 The igneous rim surrounding a type I chondrule in the Northwest Africa 3118 CV<sub>oxA</sub>  
 497 chondrite mainly consists of two types of olivine with MgO-rich (Fa<sub>11-22</sub>) and FeO-rich  
 498 (Fa<sub>40-49</sub>) compositions. The igneous rim contains secondary minerals that were formed by  
 499 aqueous alteration on the CV chondrite parent body, including ~~ferroan~~ FeO-rich olivine,  
 500 nepheline, and Fe-Ni sulfides.

501 The oxygen isotopic composition of the FeO-rich olivine ( $\delta^{17}O = 2.0 \pm 1.8\%$ ,  $\delta^{18}O$   
 502  $= 8.1 \pm 3.6\%$ , 2SD), the mass-dependent isotope fractionation, and the porous texture filling  
 503 between the MgO-rich olivine grains indicate that the FeO-rich olivine precipitated from an  
 504  $^{16}O$ -poor aqueous fluid on the CV chondrite parent body. The MgO-rich olivine shows Fe-Mg  
 505 chemical zoning at the interface with the FeO-rich olivine, indicating that Fe-Mg  
 506 inter-diffusion occurred during the aqueous alteration on the parent body. The inter-diffusion  
 507 distance indicates that the oxygen isotopic composition of the MgO-rich olivine ( $\delta^{17}O = -5.6 \pm$

508 3.2‰,  $\delta^{18}\text{O} = -0.7 \pm 3.6\text{‰}$ ) was not disturbed on the parent body and should preserve the rim  
509 formation events in the solar nebula.

510 The MgO-rich olivine includes extreme  $^{16}\text{O}$ -rich areas ( $\delta^{17,18}\text{O} \sim -30\text{‰}$ ). These  
511 areas are anhedral and less than 10  $\mu\text{m}$  across, indicating that they represent relict grains that  
512 survived the igneous rim formation event. The oxygen diffusion distance of about 1  $\mu\text{m}$  in the  
513 extreme  $^{16}\text{O}$ -rich area constrains that the heating duration of the igneous rim formation was  
514 from several hours to several days at about 2000 K, suggesting flash heating events similar to  
515 chondrule formation formed the igneous rim. The MgO-rich olivine grains with  $\delta^{18}\text{O}$  values of  
516  $\sim -1\text{‰}$  overgrew the extreme  $^{16}\text{O}$ -rich relict olivine grains during igneous rim formation.

517

### 518 **Acknowledgments**

519 This article is dedicated to Klaus Keil in honor of his outstanding contributions to  
520 cosmochemistry. Constructive comments by Timothy J. Fagan, Kazuhide Nagashima and the  
521 Associate Editor Alexander N. Krot significantly improved the quality of the manuscript. This  
522 study is partly supported by the Monbu-kagaku-sho grants.

523

### 524 **References**

525 Allen, J.S., Nozette, S., Wilkening, L.L., 1980. A study of chondrule rims and chondrule  
526 irradiation records in unequilibrated ordinary chondrites. *Geochim. Cosmochim.*  
527 *Acta* 44, 1161–1175.

528 Andersson, K., Borchardt, G., Scherrer, S., Weber, S., 1989. Self-diffusion in  $\text{Mg}_2\text{SiO}_4$   
529 (forsterite) at high temperature. *Fresen. Z. Anal. Chem.* 333, 383–385.

530 Ando, K., Kurokawa, H., Oishi, Y., 1981. Self-diffusion coefficient of oxygen in  
531 single-crystal forsterite. *J. Am. Ceram. Soc.* C-30.

532 Ashworth, J.R., 1977. Matrix textures in unequilibrated ordinary chondrites. *Earth Planet.*  
533 *Sci. Lett.* 35, 25–34.

534 Brearley, A.J., 2003. Nebular versus parent-body processing. *Treatise on Geochemistry,*  
535 *Meteorites, Comets, and Planets.*, Vol 1. Elsevier, Oxford, 247–269 (ed. by H. D.  
536 Holland and K. K. Turekian).

537 Brearley, A.J., Krot, A.N., 2013. Metasomatism in the early solar system: The record from  
538 chondritic meteorites. In *Metasomatism and the Chemical Transformation of*  
539 *Rock Lecture Notes in Earth System Sciences.* 659–789.

540 Chakraborty, S., 1997. Rates and mechanisms of Fe-Mg interdiffusion in olivine at  
541 980°C–1300°C. *J. Geophys. Res.* 102, 12317–12331.

542 Cuvillier, P., Leroux, H., Jacob, D., Hirel, P., 2015. Fe-Mg interdiffusion profiles in rimmed  
543 forsterite grains in the Allende matrix: Time-temperature constraints for the

544 parent body metamorphism. *Meteorit. Planet. Sci.* 50, 1529–1545.

545 Dohmen, R., Chakraborty, S., Becker, H.-W., 2002. Si and O diffusion in olivine and  
546 implications for characterizing plastic flow in the mantle. *Geophys. Res. Lett.* 29,  
547 26-1–26-4.

548 Dohmen, R., Becker, H.-W., Chakraborty, S., 2007. Fe-Mg diffusion in olivine I:  
549 Experimental determination between 700°C and 1,200°C as a function of  
550 composition, crystal orientation and oxygen fugacity. *Phys. Chem. Miner.* 34,  
551 389–407.

552 Dohmen, R., Chakraborty, S., 2007. Fe-Mg diffusion in olivine II: Point defect chemistry,  
553 change of diffusion mechanisms and a model for calculation of diffusion  
554 coefficients in natural olivine. *Phys. Chem. Miner.* 34, 409–430.

555 Gérard, O., Jaoul, O., 1989. Oxygen diffusion in San Carlos olivine. *J. Geophys. Res.* 94,  
556 4119–4128.

557 Gooding, J.L., Keil, K., Fukuoka, T., Schimit, R.A., 1980. Elemental abundances in  
558 chondrules from unequilibrated chondrites: Evidence for chondrule origin by  
559 melting of pre-existing materials. *Earth Planet. Sci. Lett.* 50, 171–180.

560 Grossman, J.N., Wasson, J.T., 1982. Evidence for primitive nebular components in  
561 chondrules from the Chainpur chondrite. *Geochim. Cosmochim. Acta* 46, 1081–  
562 1099.

563 Grossman, L., Fedkin, A.V., Simon S.B., 2012. Formation of the first oxidized iron in the  
564 solar system. *Meteorit. Planet. Sci.* 47, 2160–2169.

565 Hewins, R.H., 1996. Chondrules and the protoplanetary disk: an overview. In *Chondrules*  
566 *and the Protoplanetary Disk* (eds. by Hewins, R.H., Jones, R.H. and Scotte,  
567 E.R.D.), pp. 3–9. Cambridge University Press.

568 Hewins, R.H., Connolly Jr., H.C., Lofgren, G.E., Libourel, G., 2005. Experimental  
569 constraints on chondrule formation. In *Chondrites and the Protoplanetary Disk*  
570 (eds. by Krot, A.N., Scott, E.R.D. and Reipurth, B.) ASP Conference Series 341.  
571 pp. 286–316.

572 Huss, G.R., Rubin, A.E., Grossman, J.N., 2006. Thermal metamorphism in chondrites. In  
573 *Meteorites and the Early Solar System II* (eds. by Lauretta, D.S. and McSween,  
574 H.Y.), pp. 567-586. University of Arizona, Houston.

575 Ito, M., Messenger, S., 2010. Thermal metamorphic history of a Ca, Al-rich inclusion  
576 constrained by high spatial resolution Mg isotopic measurements with  
577 NanoSIMS 50L. *Meteorit. Planet. Sci.* 45, 583–595.

578 Jaoul, O., Froidevaux, C., Durham, W.B., Michaut, M., 1980. Oxygen self-diffusion in  
579 forsterite: Implications for the high-temperature creep mechanism. *Earth Planet.*

580 Sci. Lett. 47, 391–397.

581 Jaoul, O., Houlier, B., Abel, F., 1983. Study of  $^{18}\text{O}$  diffusion in magnesium orthosilicate by  
582 nuclear microanalysis. *J. Geophys. Res.* 88, 613–624.

583 Keil, K., 2000. Thermal alteration of asteroids: evidence from meteorites. *Planet. Space Sci.*  
584 48, 887–903.

585 King, T.V.V., King, E.A., 1981. Accretionary dark rims in unequilibrated chondrites. *Icarus*  
586 48, 460–472.

587 Komatsu, M., Fagan, T.J., Mikouchi, T., Petaev, M.I., Zolensky M.E., 2015. LIME silicates  
588 in amoeboid olivine aggregates in carbonaceous chondrites: Indicator of nebular  
589 and asteroidal processes. *Meteorit. Planet. Sci.* 50, 1271–1294.

590 Krot, A.N., Wasson, J.T., 1995. Igneous rims on low-FeO and high-FeO chondrules in  
591 ordinary chondrites. *Geochim. Cosmochim. Acta* 59, 4951–4966.

592 Krot, A.N., Scott, E.R.D., Zolensky, M.E., 1995. Mineralogical and chimerical modification  
593 of components in CV3 chondrites: Nebular or asteroidal processing? *Meteoritics*  
594 30, 748–776.

595 Krot, A.N., Petaev, M.I., Scott, E.R.D., Choi, B.-G., Zolensky, M.E., Keil, K., 1998.  
596 Progressive alteration in CV3 chondrites: More evidence for asteroidal alteration.  
597 *Meteorit. Planet. Sci.* 33, 1065–1085.

598 Krot, A.N., Petaev, M.I., Bland, P.A., 2004. Multiple formation mechanisms of ferrous  
599 olivine in CV carbonaceous chondrites during fluid-assisted metamorphism.  
600 *Antarc. Meteorite Res.* 17, 153–171.

601 Kunihiro, T., Nagashima, K., Takayanagi, I., Nakamura, J., Kosaka, K., Yurimoto, H. 2001.  
602 Noise characteristics of stacked CMOS active pixel sensor for charged particles.  
603 *Nucl. Instrum. Methods Phys. Res.* 470, 512–519.

604 Maruyama, S., Yurimoto, H., Sueno, S., 1999. Oxygen isotope evidence regarding the  
605 formation of spinel-bearing chondrules. *Earth Planet. Sci. Lett.* 169, 165–171.

606 Maruyama, S., Yurimoto, H., 2003. Relationship among O, Mg isotopes and the petrography  
607 of two spinel-bearing compound chondrules. *Geochim. Cosmochim. Acta* 67,  
608 3943–3957.

609 Matsumoto, K., Yurimoto, H., Kosaka, K., Miyata, K., Nakamura, T., Sueno, S., 1993. A  
610 novel ion imager for secondary ion mass spectrometry. *IEEE Trans. Electron*  
611 *Devices* 40, 82–85.

612 Myers, J., Eugster, H.P., 1983. The system Fe-Si-O: oxygen buffer calibrations to 1,500 K.  
613 *Contrib. Mineral. Petrol.* 82, 75–90.

614 Nagashima, K., Kunihiro, T., Takayanagi, I., Nakamura, J., Kosaka, K., Yurimoto, H., 2001  
615 Output characteristics of stacked CMOS-type active pixel sensor for charged

616 particles. *Surf. Interface Anal.* 31, 131–137.

617 Nagashima, K., Takeda, Y., Itoh, S., Yurimoto, H., 2003.  $^{16}\text{O}$ -rich olivine in igneous rim of  
618 type I chondrule from CR2 chondrite. 66th Annual meeting of the Meteoritical  
619 Society, 5140 (abstract).

620 Nagashima, K., Krot, A.N., Huss, G.R., 2011. Oxygen-Isotope Compositions of Chondrules  
621 and Matrix Grains in Kakangari Chondrite. Workshop on Formation of the First  
622 Solids in the Solar System, 9049 (abstract).

623 Nagashima, K., Krot, A.N., Libourel, G., Huss, G.R., 2013. Magnesian porphyritic  
624 chondrules surrounded by ferroan igneous rims from CR chondrite GRA 95229.  
625 44th Lunar and Planetary Science Conference, 1780 (abstract).

626 Nagashima, K., Krot, A.N., Huss, G.R., 2015. Oxygen-isotope compositions of chondrule  
627 phenocrysts and matrix grains in Kakangari K-grouplet chondrite: Implication to  
628 a chondrule-matrix genetic relationship. *Geochim. Cosmochim. Acta* 151, 49–67.

629 Nakamura, A., Schmalzried, H., 1984. On the  $\text{Fe}^{2+}$ - $\text{Mg}^{2+}$ -interdiffusion in olivine (II). *Ber.*  
630 *Bunsenges. Phys. Chem.* 88, 140–145.

631 Oishi, Y., Ando, K., 1984. Oxygen self-diffusion coefficient in single-crystal forsterite. In  
632 *Materials Science of the Earth's Interior* (ed. by Sunagawa, I.). Terra Science  
633 Publishing Company, Tokyo, Japan, pp. 271–280.

634 Park, C., Wakaki, S., Sakamoto, N., Kobayashi, S., Yurimoto, H., 2012. Oxygen isotopic  
635 composition of the solar nebula gas inferred from high-precision isotope imaging  
636 of melilite crystals in an Allende CAI. *Meteorit. Planet. Sci.* 47, 2070–2083.

637 Reddy, K.P.R., Oh, S.M., Major Jr., L.D., Cooper, A.R., 1980. Oxygen diffusion in forsterite.  
638 *J. Geophys. Res.* 85, 322–326.

639 Righter, K., Neff, K.E., 2007. Temperature and oxygen fugacity constraints on CK and R  
640 chondrites and implications for water and oxidation in the early solar system.  
641 *Polar science* 1, 25–44.

642 Russell, S.S., Zolensky, M., Righter, K., Folco, L., Jones, R., Connolly Jr., H.C., Grady,  
643 M.M., Grossman, J.N., 2005. *The Meteoritical Bulletin*, No. 89, 2005 September.  
644 *Meteorit. Planet. Sci.* 40, 201–263.

645 Rubin, A.E., 1984. Coarse-grained chondrule rims in type 3 chondrites. *Geochim.*  
646 *Cosmochim. Acta* 48, 1779–1789.

647 Rubin, A.E., Wasson, J.T., 1987. Chondrules, matrix and coarse-grained chondrule rims in  
648 the Allende meteorite: Origin, interrelationships, and possible precursor  
649 components. *Geochim. Cosmochim. Acta* 51, 1923–1937.

650 Ryerson, F.J., Durham, W.B., Cherniak, D.J., Lanford, W.A., 1989. Oxygen diffusion in  
651 olivine: Effect of oxygen fugacity and implications for creep, *J. Geophys. Res.* 94,

652 4105–4118.

653 Sakamoto, N., Yurimoto, H., 2006. Highly sensitive ion imaging system using direct  
654 combination of a stacked-type solid-state imager and a microchannel plate driven  
655 by LabVIEW software. *Surf. Interface Anal.* 38, 1760–1762.

656 Sakamoto, N., Seto, Y., Itoh, S., Kuramoto, K., Fujino, K., Nagashima, K., Krot, A.N.,  
657 Yurimoto, H., 2007. Remnants of the early solar system water enriched in heavy  
658 oxygen isotopes. *Science* 317, 231–233.

659 Scott, E.R.D., Rubin, A.E., Taylor, G.J., Keil, K., 1984. Matrix material in type 3 chondrites  
660 - Occurrence, heterogeneity and relationship with chondrules. *Geochim.*  
661 *Cosmochim. Acta* 48, 1741–1757.

662 Soulié, C., Libourel, G., Tissandier, L., 2017. Olivine dissolution in molten silicates: An  
663 experimental study with application to chondrule formation. *Meteorit. Planet. Sci.*  
664 52, 225–250.

665 Tachibana, S., Tamada, S., Kawasaki, H., Ozawa, K., Nagahara, H., 2013. Interdiffusion of  
666 Mg-Fe in olivine at 1,400-1,600 °C and 1 atm total pressure. *Phys. Chem. Miner.*  
667 40, 511–519.

668 Takayanagi, I., Nakamura, J., Fossum, E.R., Nagashima, K., Kunihiro, T., Yurimoto, H.,  
669 2003. Dark current reduction in stacked-type CMOS-APS for charged particle  
670 imaging. *IEEE Trans. Electron Devices* 70–76.

671 Takeda, Y., Itoh, S., Yurimoto, H., 2002. Oxygen isotopic composition in a CR chondrule.  
672 Japan Geoscience Union Meeting (abstract).

673 Tenner, T.J., Nakashima, D., Ushikubo, T., Kita N.T., Weisberg, M.K., 2015. Oxygen isotope  
674 ratios of FeO-poor chondrules in CR3 chondrites: Influence of dust enrichment  
675 and H<sub>2</sub>O during chondrule formation. *Geochim. Cosmochim. Acta* 148, 228–250.

676 Tenner, T.J., Ushikubo, T., Nakashima, D., Schrader, D.L., Weisberg, M.K., Kimura, M.,  
677 Kita N.T., 2018. Oxygen isotope characteristics of chondrules from recent studies  
678 by secondary ion mass spectrometry. In *Chondrules* (eds. by Russell, S.S.,  
679 Connolly Jr, H.C., Krot, A.N.), pp. 196–246, Cambridge University Press.

680 Weinbruch, S., Armstrong, J., Palme, H., 1994. Constraints on the thermal history of the  
681 Allende parent body as derived from olivine-spinel thermometry and Fe/Mg  
682 interdiffusion in olivine. *Geochim. Cosmochim. Acta* 58, 1019–1030.

683 Yamamoto, K., Sakamoto, N., Yurimoto, H., 2010. Analysis of the noise properties of a  
684 solid-state SCAPS ion imager and development of software noise reduction. *Surf.*  
685 *Interface Anal.* 42, 1603–1605.

686 Yurimoto, H., Nagashima, K., Kunihiro, T., 2003. High precision isotope micro-imaging of  
687 materials. *Appl. Surf. Sci.* 203-204, 793–797.

688 Yurimoto, H., Krot, A.N., Choi, B.-G., Aléon, J., Kunihiro, T., Brearley, A.J., 2008. Oxygen  
689 isotopes in chondritic components. In *Oxygen in the Solar System* (ed. by  
690 MacPherson, G.J.). *Reviews in Mineralogy and Geochemistry*, vol. 68.  
691 Mineralogical Society of America, Washington, DC. pp. 141–186.

692 Yurimoto, H., Abe, K., Abe, M., Ebihara, M., Fujimura, A., Hashiguchi, M., Hashizume, K.,  
693 Ireland, T.R., Itoh, S., Katayama, J., Kato, C., Kawaguchi, J., Kawasaki, N.,  
694 Kitajima, F., Kobayashi, S., Meike, T., Mukai, T., Nagao, K., Nakamura, T.,  
695 Naraoka, H., Noguchi, T., Okazaki, R., Park, C., Sakamoto, N., Seto, Y., Takei,  
696 M., Tsuchiyama, A., Uesugi, M., Wakaki, S., Yada, T., Yamamoto, K., Yoshikawa,  
697 M., Zolensky, M.E. 2011. Oxygen isotopic compositions of asteroidal materials  
698 returned from Itokawa by the Hayabusa mission. *Science* 333, 1116–1119.

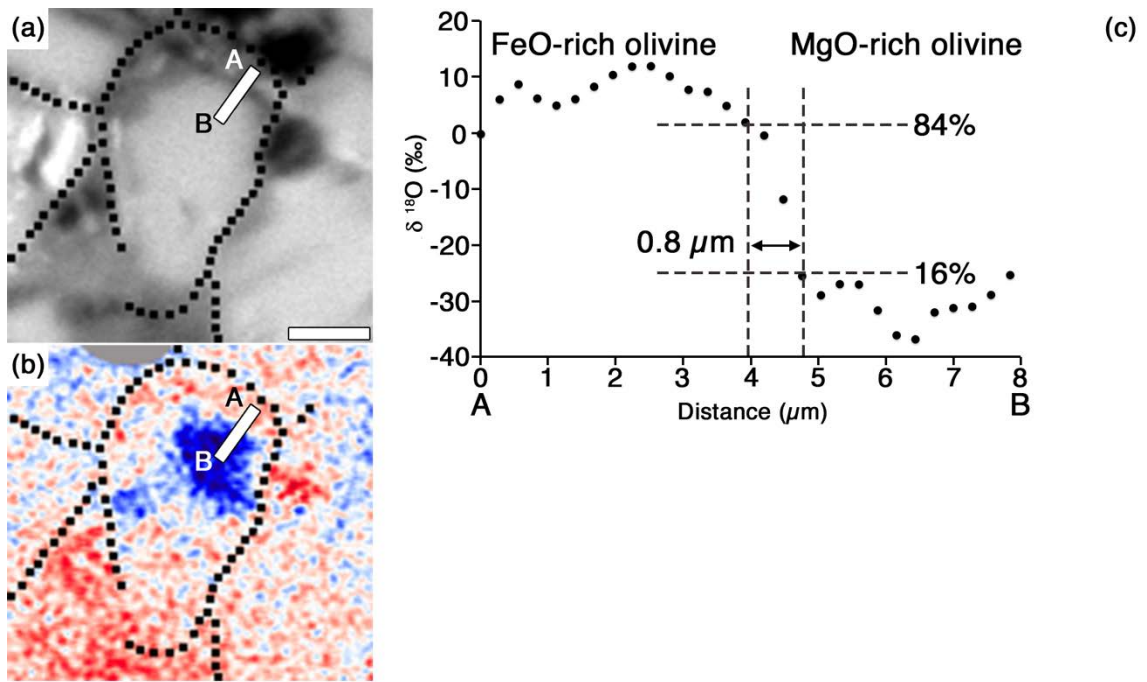
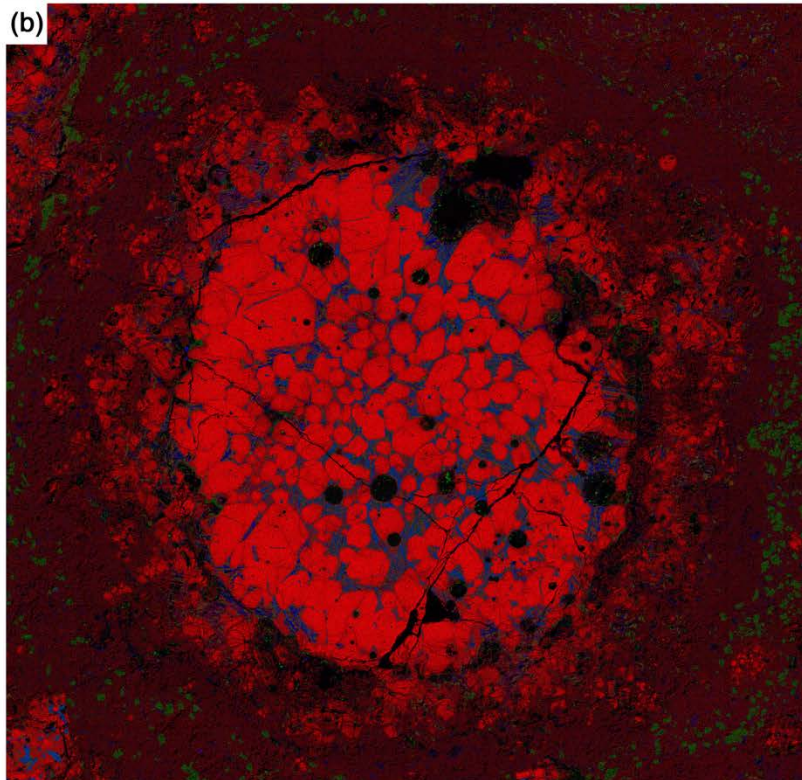
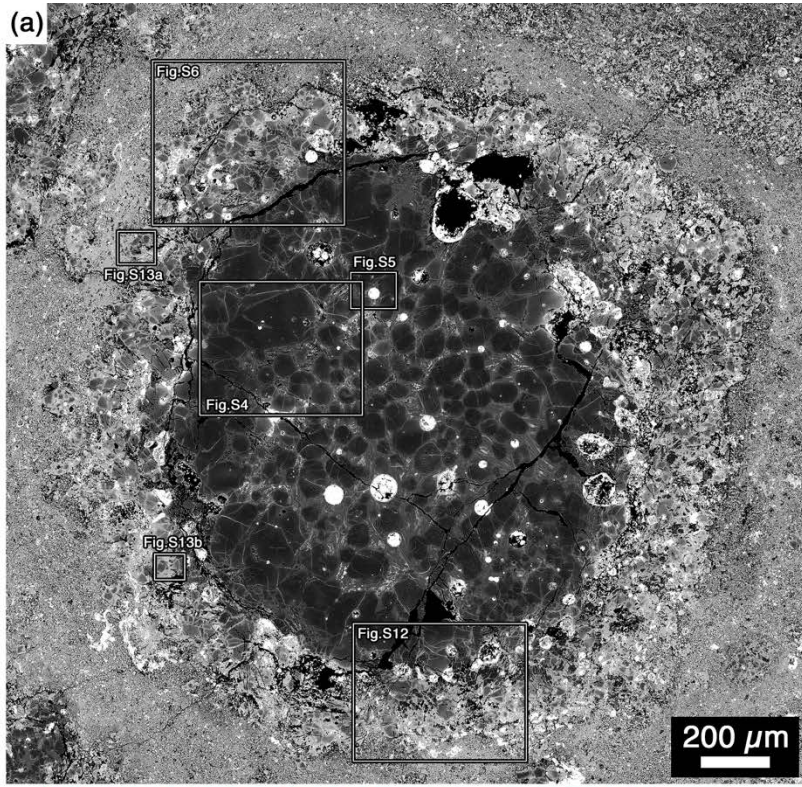


Fig. 1. (a)  $^{24}\text{Mg}^{16}\text{O}^-$  isotopograph. (b)  $\delta^{18}\text{O}$  isotopograph. (c)  $\delta^{18}\text{O}$  profile along line A-B between the MgO-rich and FeO-rich olivine. The same isotopographs are used in Fig. 7c to determine the  $\delta^{18}\text{O}$  profile within the MgO-rich olivine. Scale bar is 10  $\mu\text{m}$ .



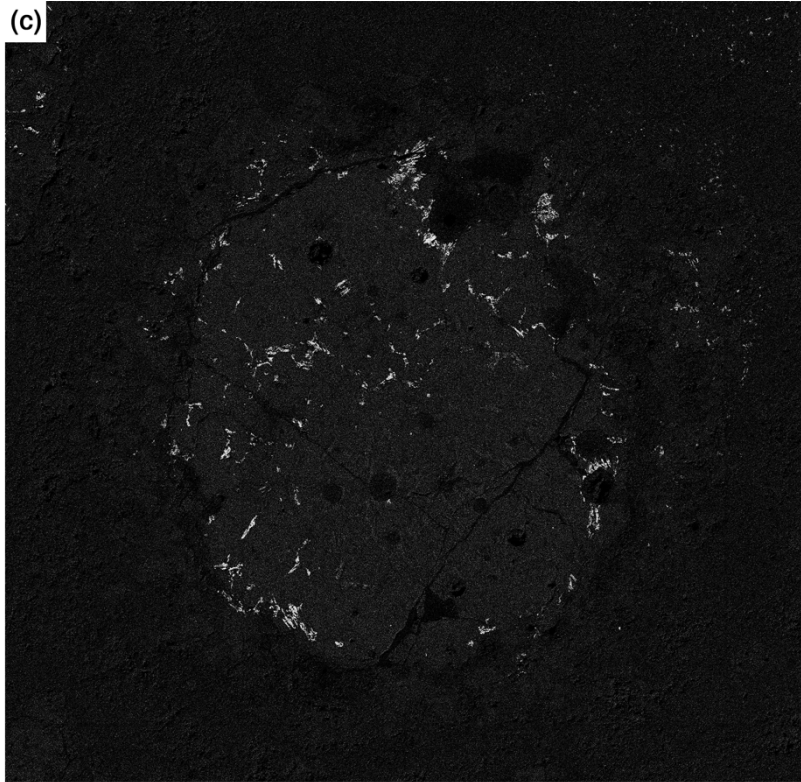


Fig. 2. (a) Back-scattered electron image of a type I chondrule surrounded by the igneous rim in the NWA3118 CV<sub>oxA</sub> chondrite. The chondrule mainly consists of olivine, mesostasis, magnetite, sulfide and Fe-Ni metal. The areas outlined by squares are enlarged and shown in the figures indicated. (b) Combined X-ray elemental map of K $\alpha$  lines of Mg (red), Ca (green), and Al (blue). Blue-colored areas are mainly composed of plagioclase and nepheline. (c) X-ray elemental map of Na K $\alpha$ . White-colored areas are nepheline-rich.

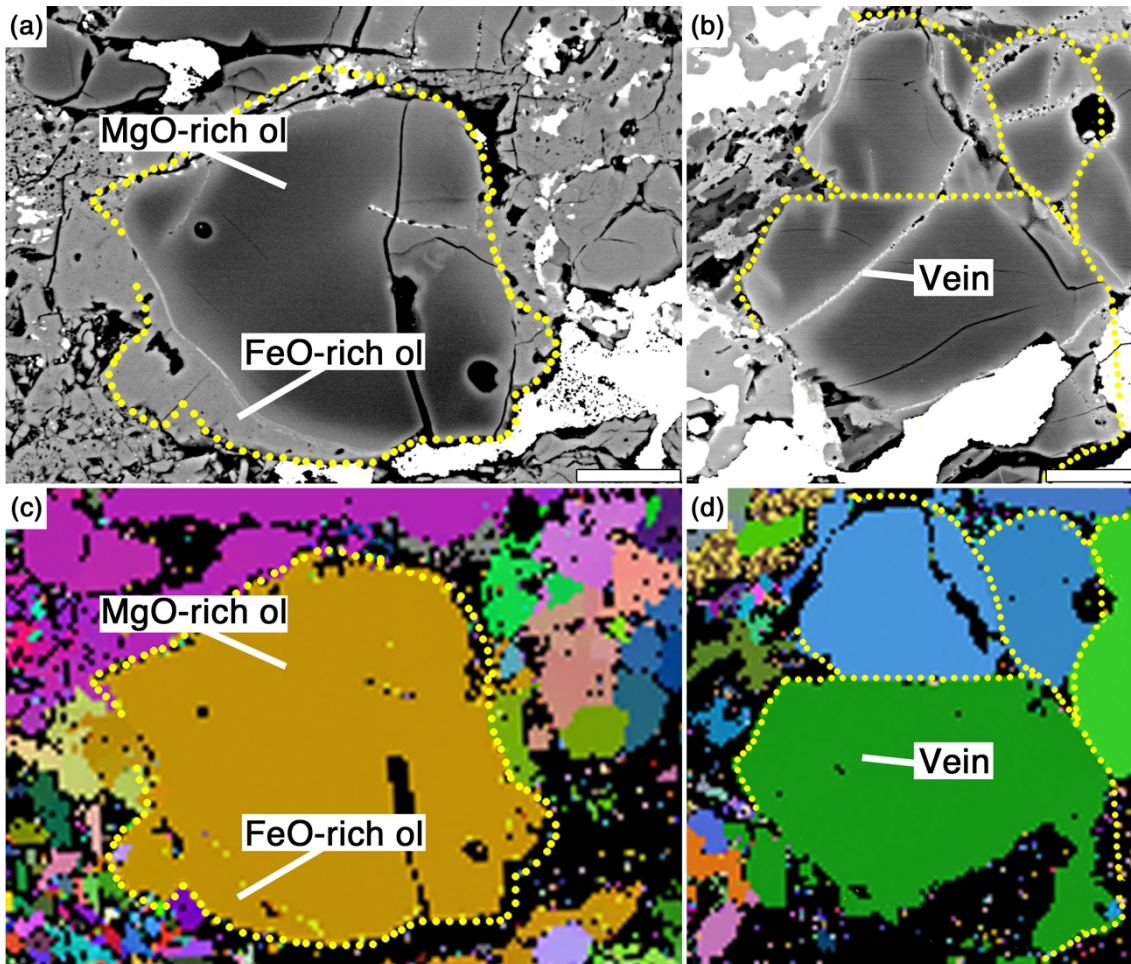
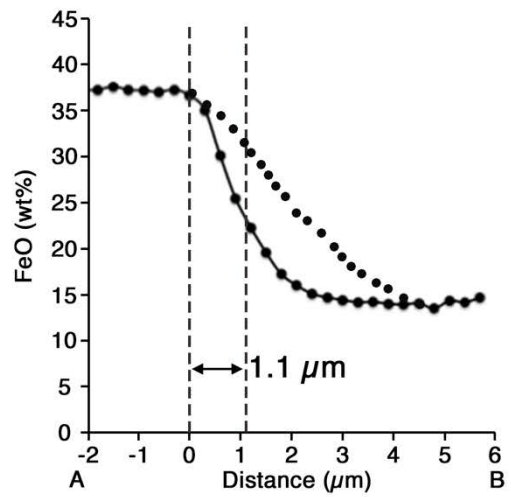
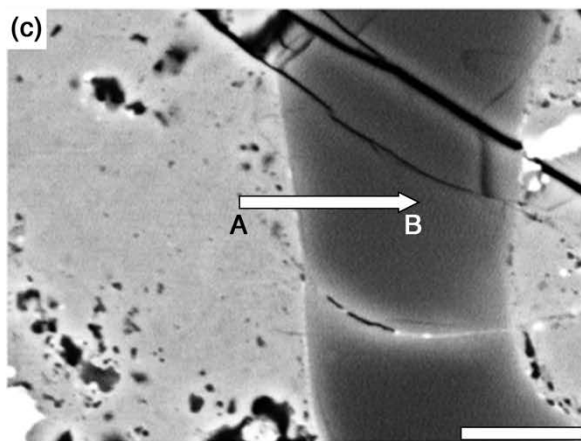
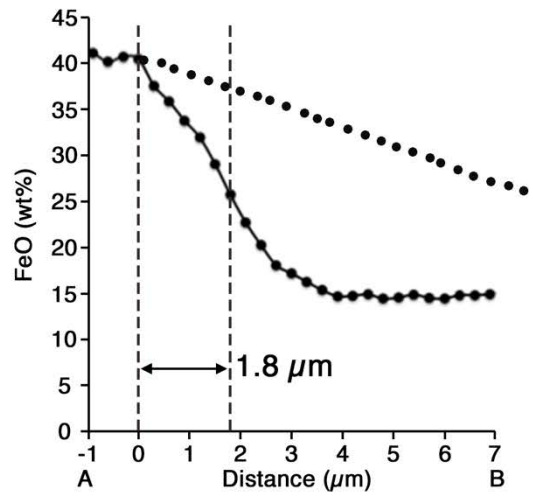
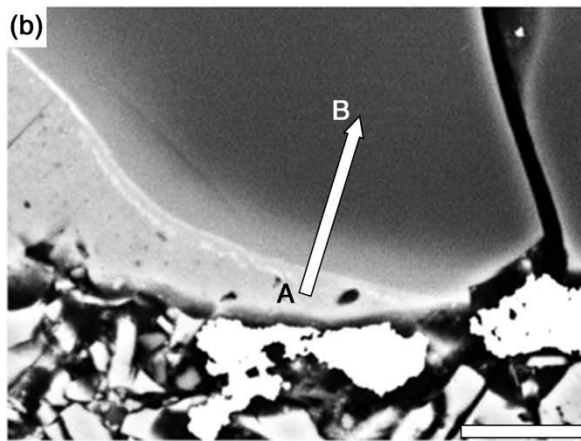
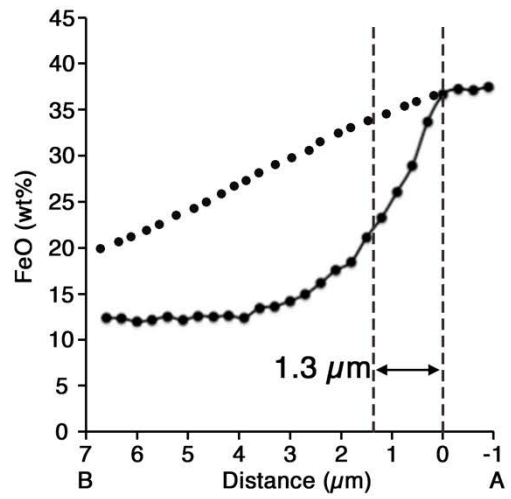
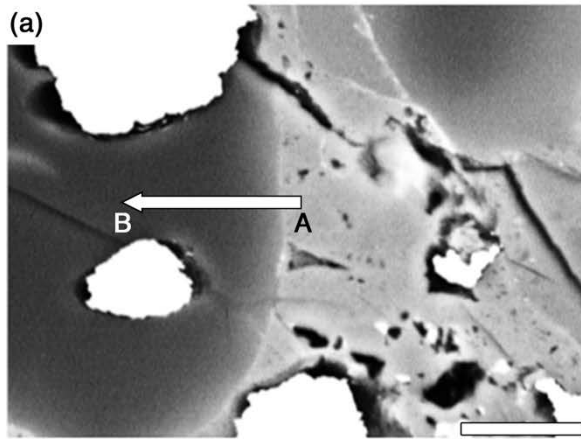
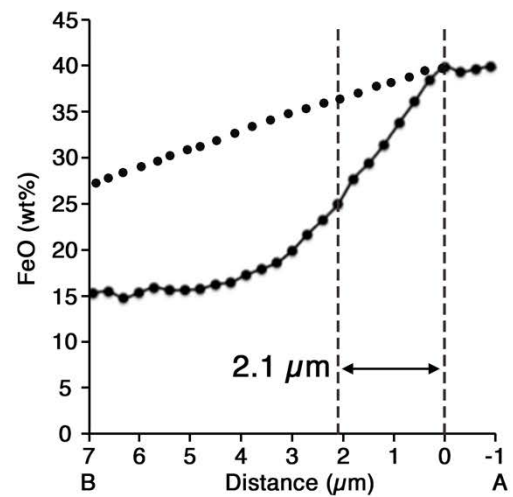
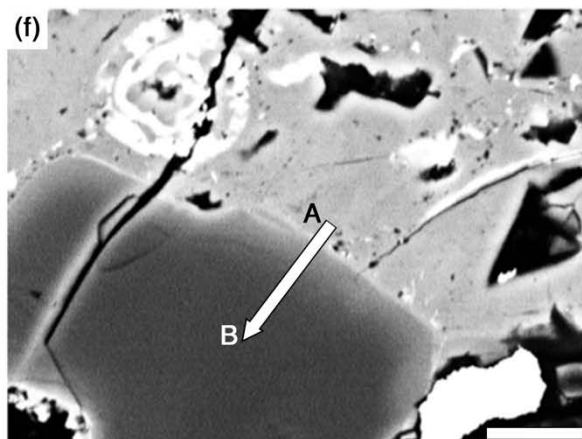
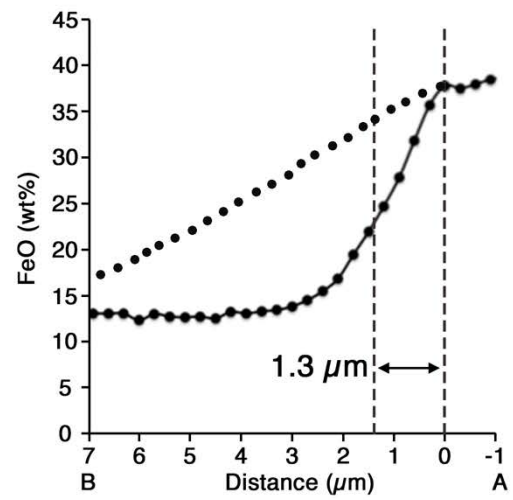
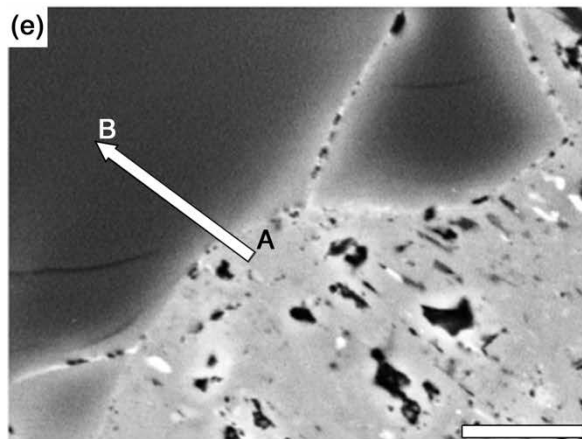
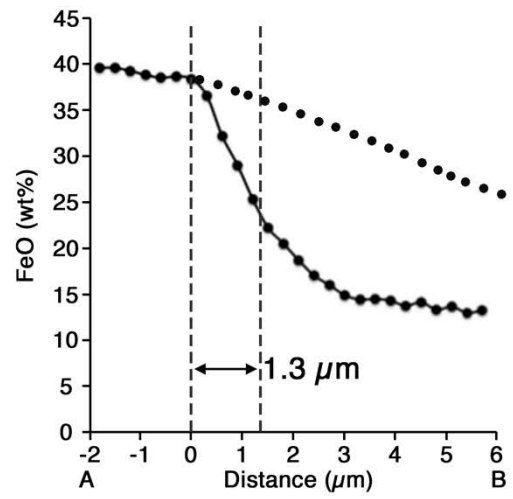
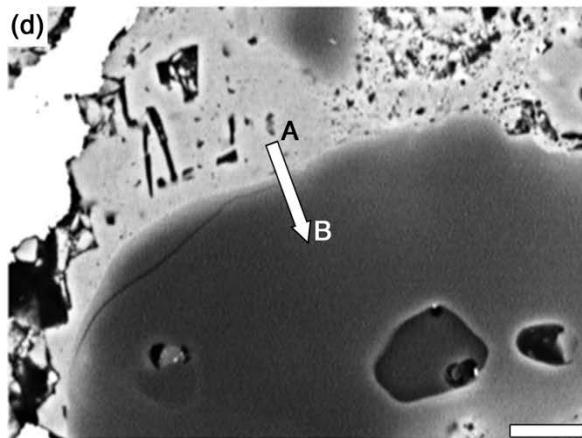


Fig. 3. Back-scattered electron images (a and b) and the EBSD images (c and d) of olivine grains in the igneous rim. Dotted lines represent grain boundaries. Scale bar is 10  $\mu\text{m}$ . In (c), the EBSD images show that the FeO-rich olivine (FeO-rich ol) and MgO-rich olivine have the same crystallographic orientation. In (d), the MgO-rich olivine grains separated by veins have the same crystallographic orientation.





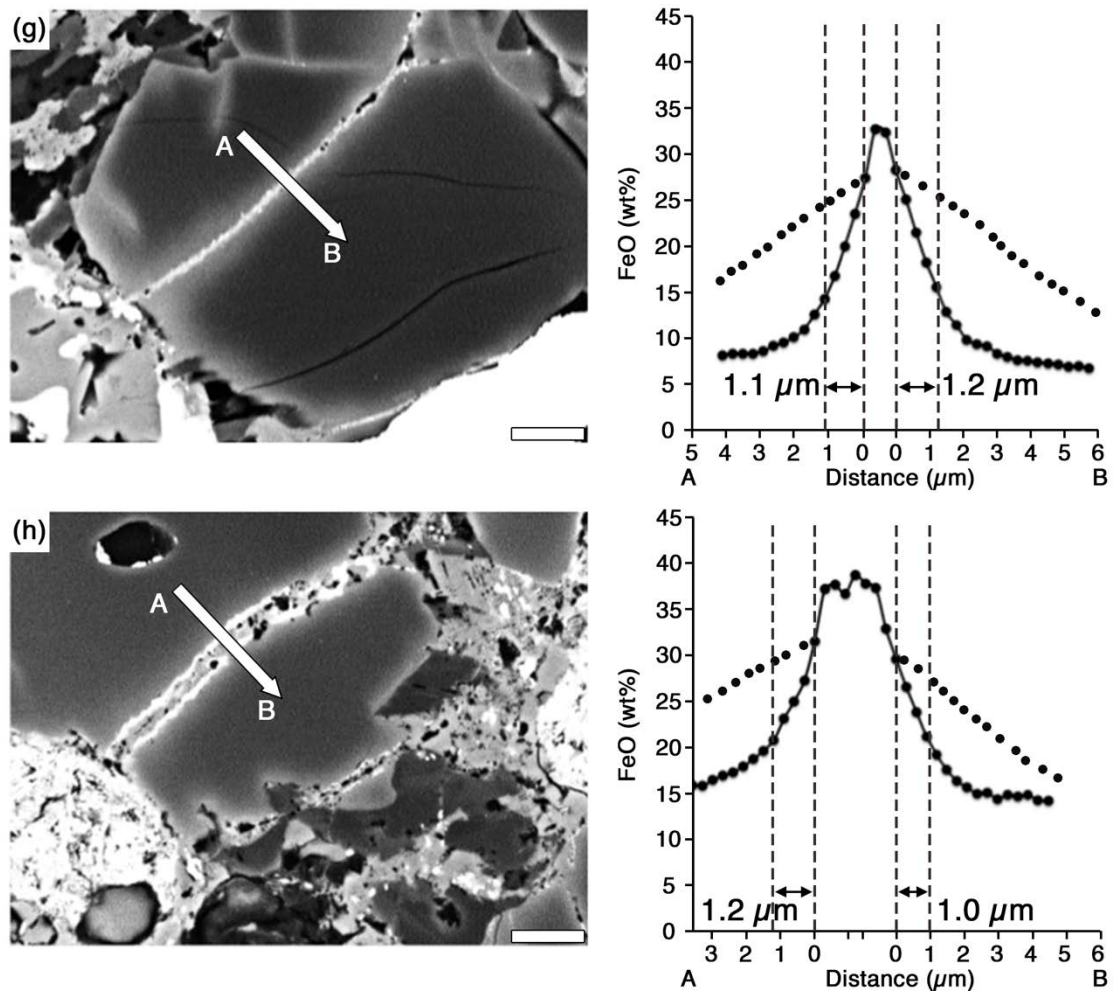


Fig. 4. (a–f) Compositional profiles along lines crossing the interfaces between FeO-rich olivine (A) and MgO-rich olivine (B). (g–h) Compositional profile across veins in MgO-rich olivine. Interdiffusion distances of the Fe-Mg zoning are shown in diagrams. Hypothetical interdiffusion profiles are shown by dotted lines in each diagram. The hypothetical diffusion is calculated using a spherical body model of constant surface concentration (Crank, 1975). The boundary conditions are as follows: initial concentration is  $Fa_2$  and the final concentration at the center of spherule is  $Fa_{15}$ . Measured surface concentration and measured radius for each olivine are used for calculation. Scale bar is 5  $\mu\text{m}$ .

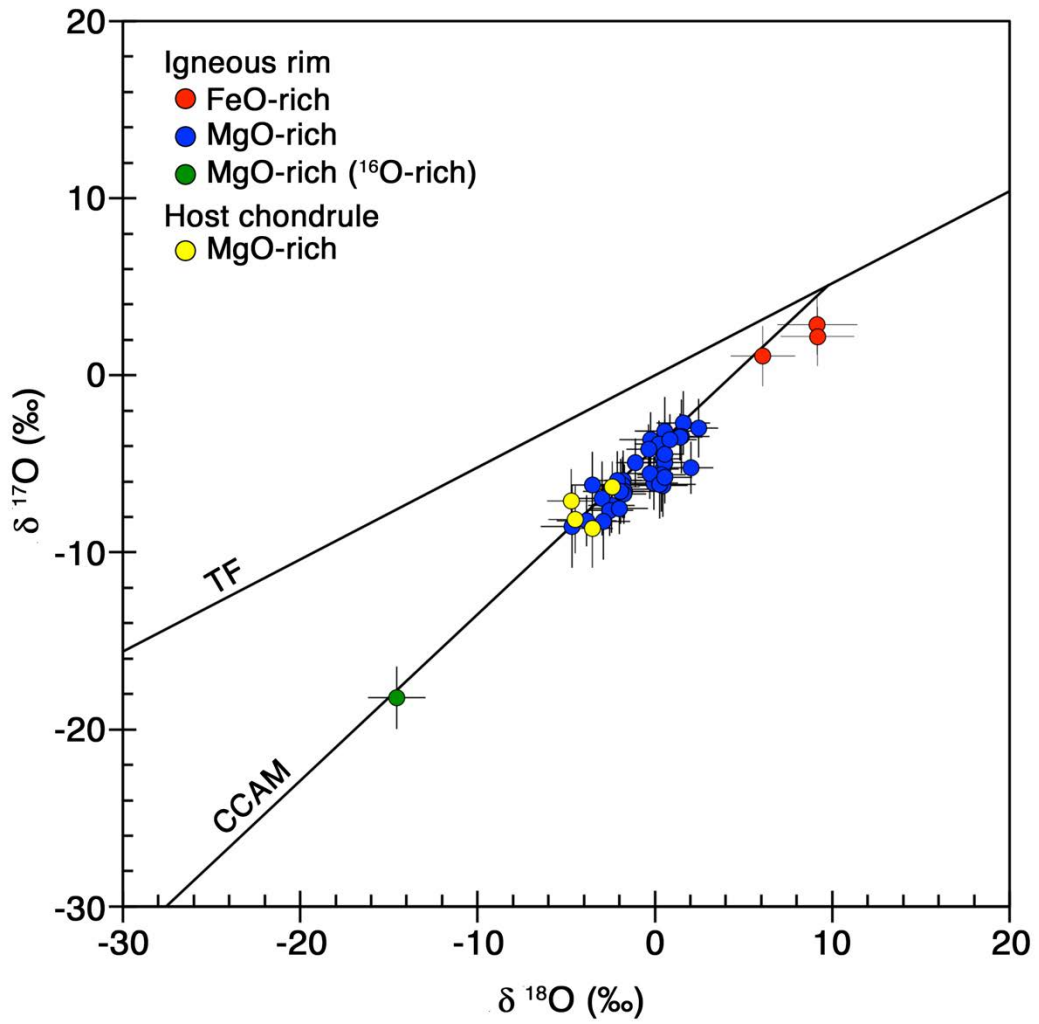


Fig. 5. Oxygen isotopic compositions of olivine in the igneous rim and the host chondrule. Error bar is  $2\sigma$  TF: terrestrial fractionation line. CCAM: carbonaceous chondrite anhydrous mineral line.

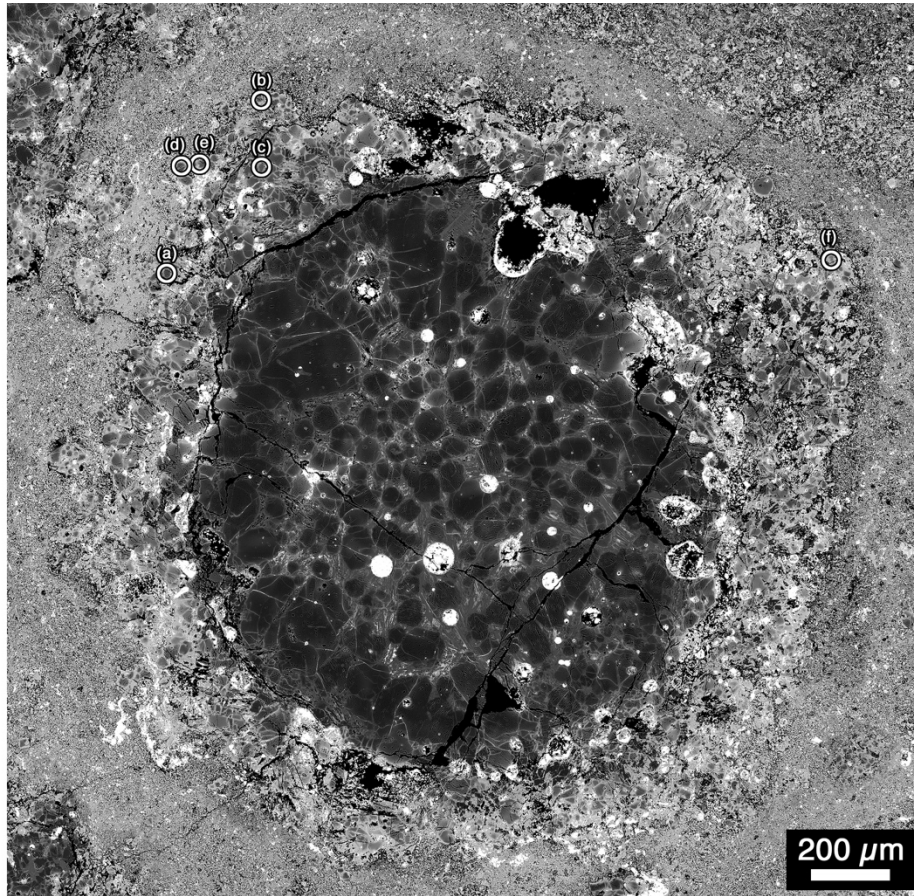


Fig. 6. Distribution of olivine grains containing the extreme  $^{16}\text{O}$ -rich areas in the igneous rim. White circles show their positions. The magnified images at locations of circles labeled (a) to (f) show in Fig. 7 with the same labels.

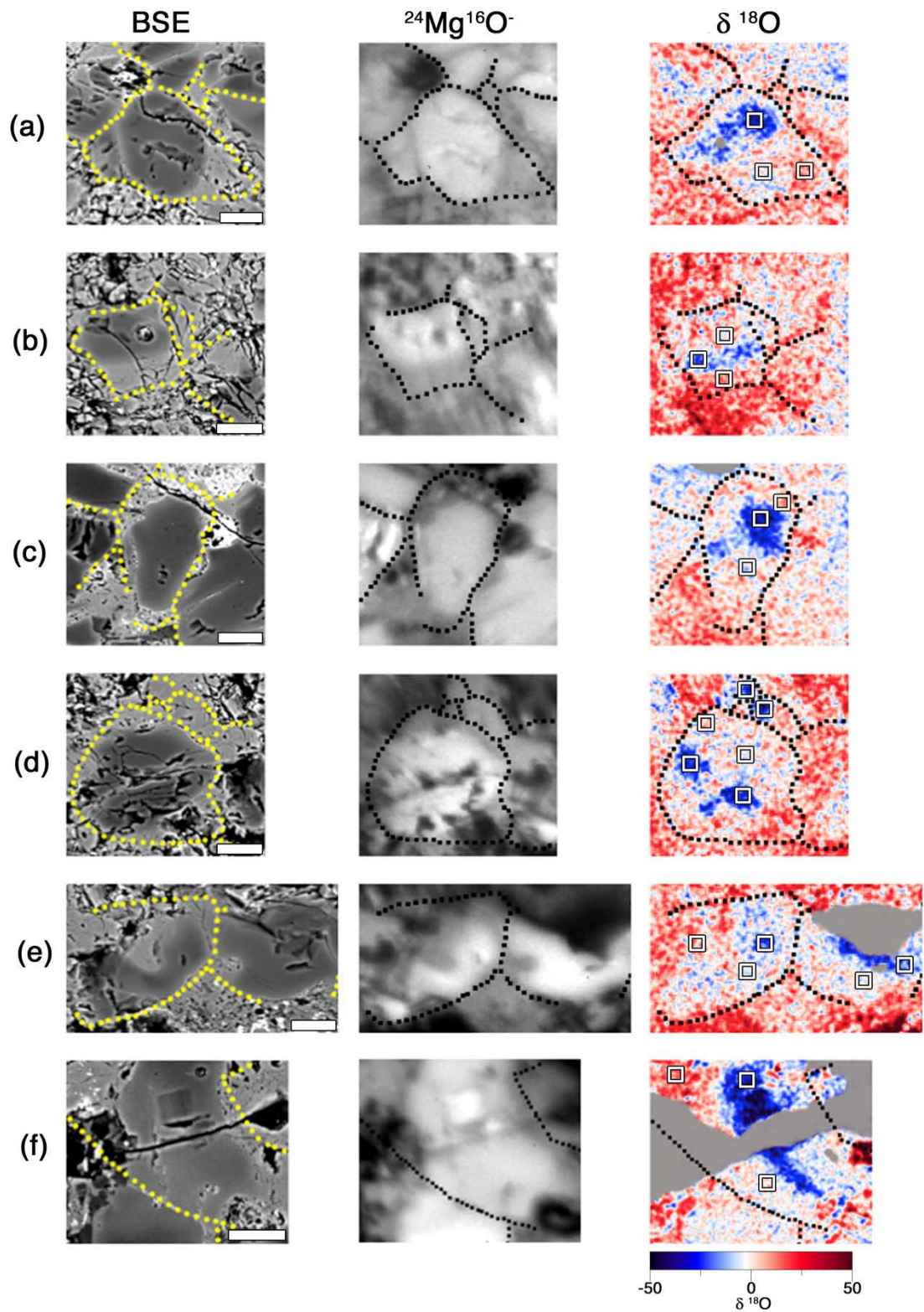


Fig. 7. BSE images,  $^{24}\text{Mg}^{16}\text{O}^-$  and  $\delta^{18}\text{O}$  isotopograph of olivine containing extreme  $^{16}\text{O}$ -rich areas in the igneous rim. Dotted lines represent the grain boundaries determined by EBSD. Scale bar is 10  $\mu\text{m}$ . Areas with artifacts are masked by the gray color. Squares in the  $\delta^{18}\text{O}$  isotopograph correspond to areas where  $\delta^{18}\text{O}$  values were calculated (see details in the text).

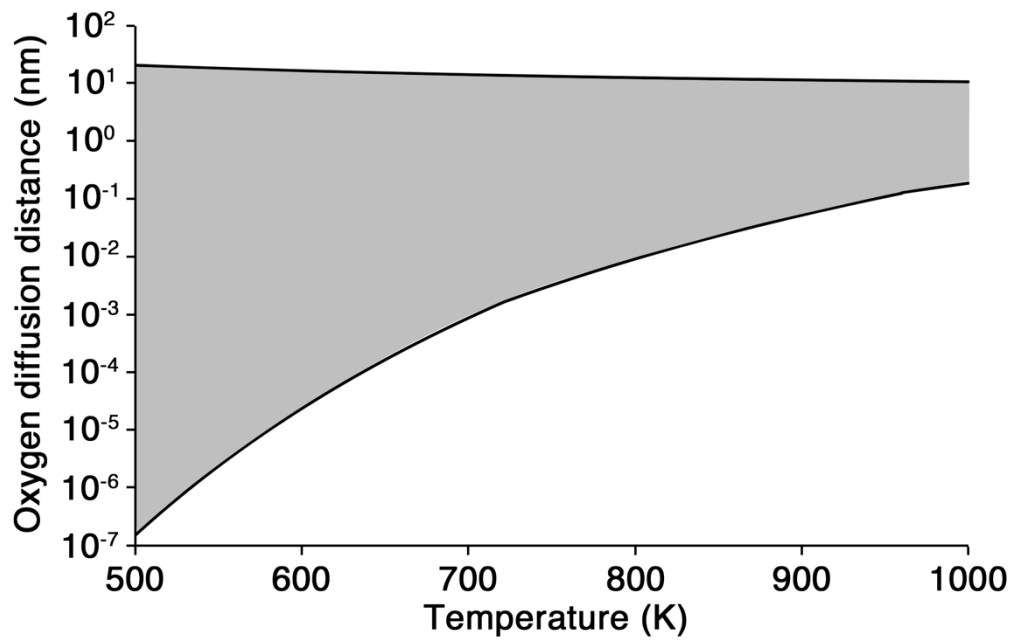


Fig. 8. Range of oxygen self-diffusion distance (nm) as a function of temperature (K) at Fe-Mg inter-diffusion distance of  $1.3 \mu\text{m}$ .

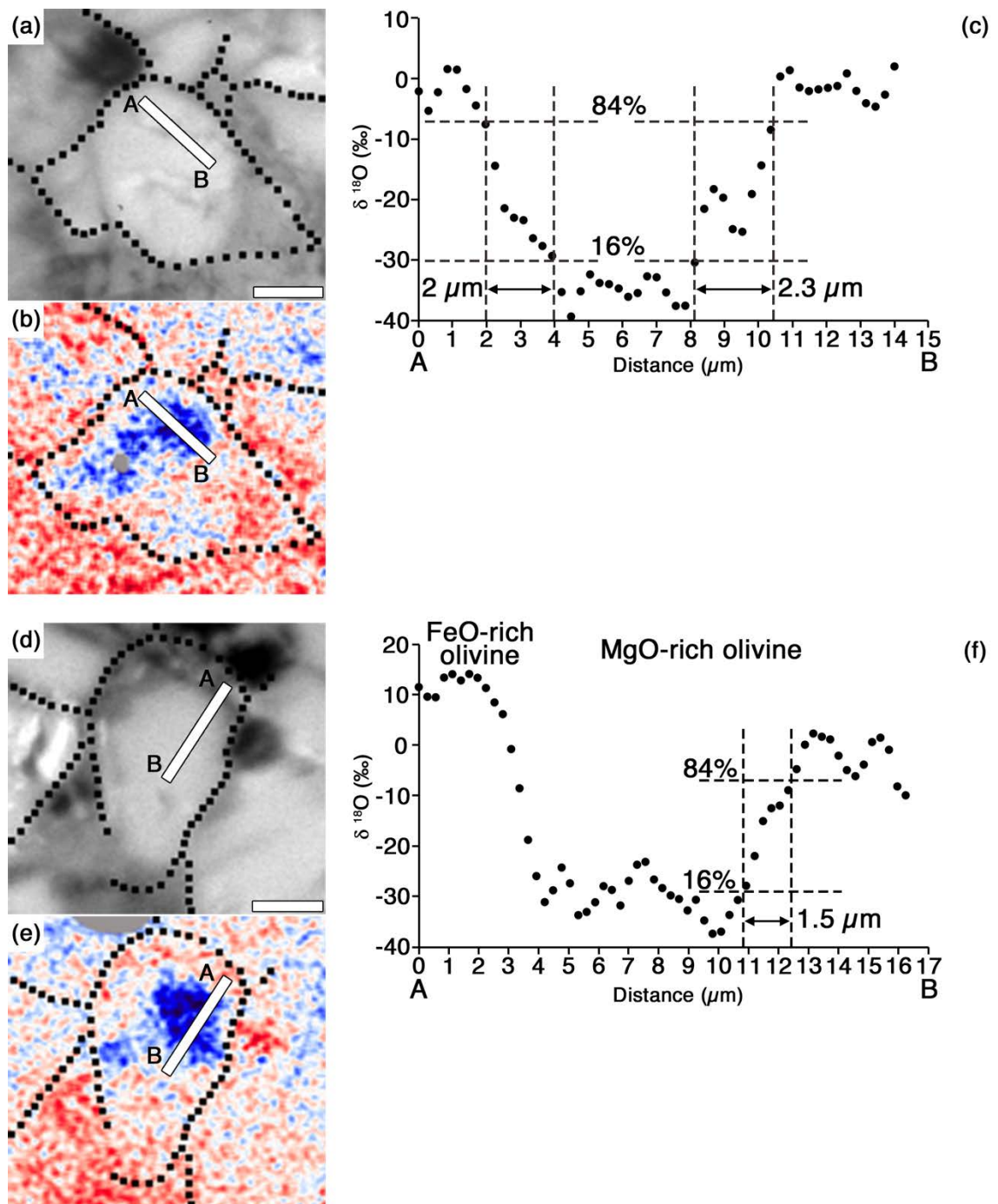


Fig. 9. (a and d)  $^{24}\text{Mg}^{16}\text{O}^-$  isotopographs; (b and e)  $\delta^{18}\text{O}$  isotopographs; (c and f)  $\delta^{18}\text{O}$  profiles of lines A-B. Scale bar is 10  $\mu\text{m}$ .

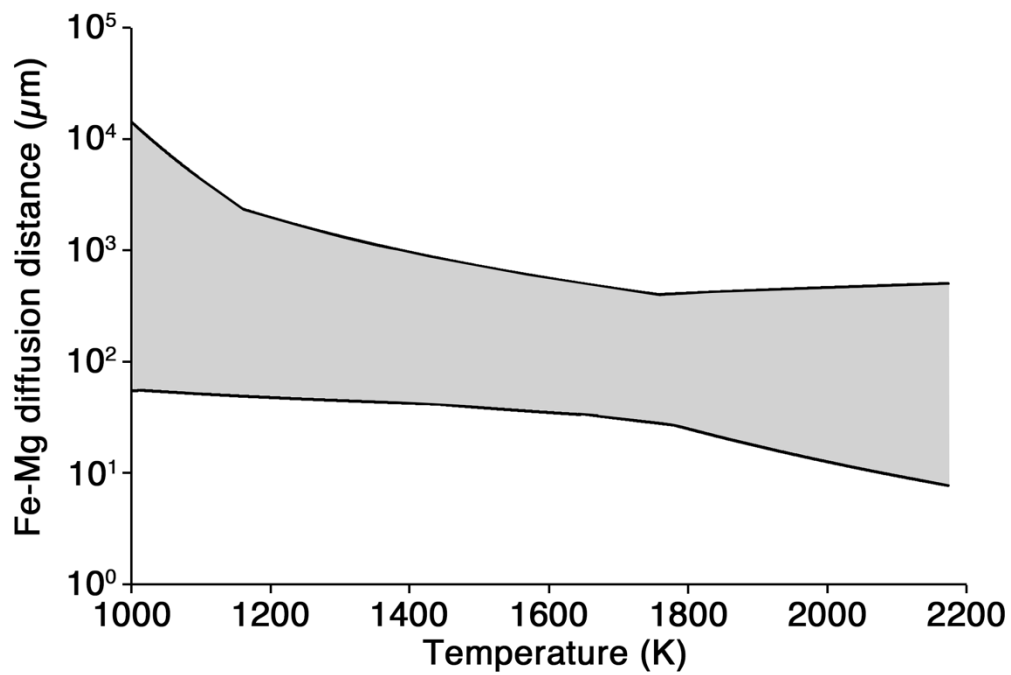


Fig. 10. Range of Fe-Mg interdiffusion distance ( $\mu\text{m}$ ) as a function of temperature (K) at oxygen self-diffusion distance of 1  $\mu\text{m}$ .

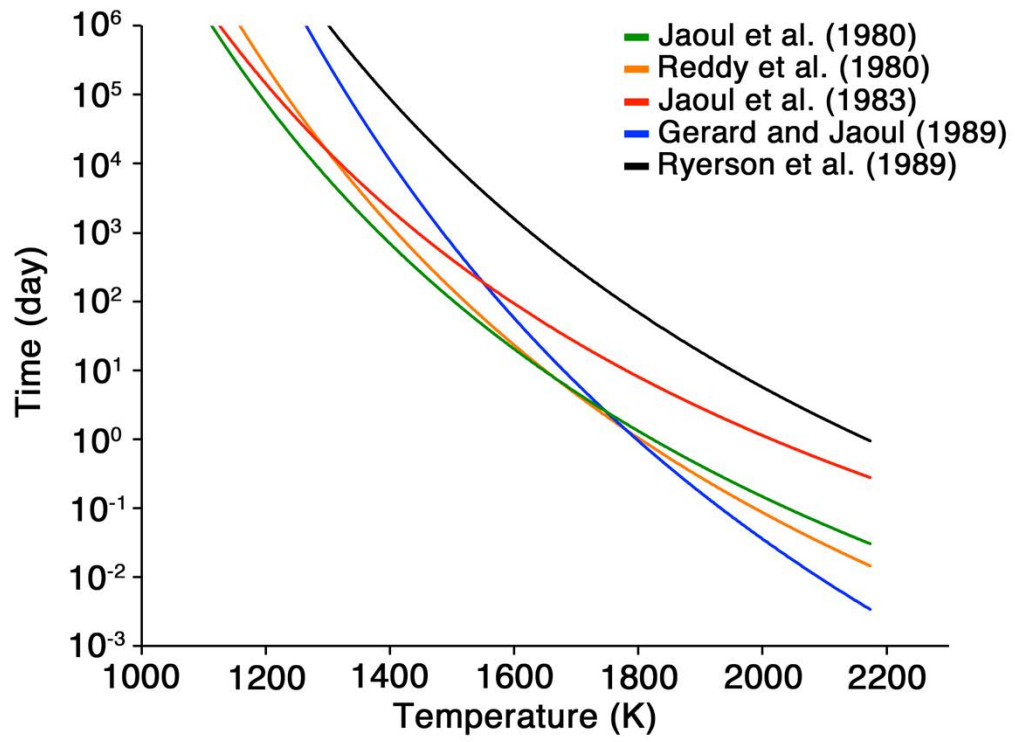


Fig. 11. Range of heating time (day) as a function of temperature (K) at oxygen self-diffusion distance of 1  $\mu\text{m}$ .